A Non-Singular Integral Equation Formulation of Permeable Semi-Infinite Hydraulic Fractures Driven by Shear-Thinning Fluids

by

Daniel Gomez

B.Eng. and B.Sc. (Hons.), University of Saskatchewan, 2014

A THESIS SUBMITTED IN PARTIAL FULFILLMENT OF

THE REQUIREMENTS FOR THE DEGREE OF

MASTER OF SCIENCE

in

THE FACULTY OF GRADUATE AND POSTDOCTORAL STUDIES

(Mathematics)

The University of British Columbia

(Vancouver)

August 2016

Abstract

This thesis considers the problem of semi-infinite hydraulic fractures driven by shear-thinning power-law fluids through a permeable elastic medium. In the recent work of Dontsov and Peirce [6], the authors reformulated the governing equations in a way that avoids singular integrals for the case of a Newtonian fluid. Moreover, the authors constructed an approximating ODE whose solutions accurately describe the fracture opening at little to no computational cost. The present thesis aims to extend their work to the more general case where the fracture is driven by a shear-thinning power-law fluid.

In the first two chapters of this thesis we outline the relevant physical modelling, and discuss the asymptotic propagation regimes typically encountered in hydraulic fracturing problems. This is followed by Chapters 4 and 5 where we reformulate the governing equations as a non-singular integral equation, and then proceed to construct an approximating ODE. In the final chapter we construct a numerical scheme for solving the non-singular integral equation. Solutions obtained in this way are then used to gauge the accuracy of solutions obtained by solving the approximating ODE.

The most important results of this thesis center on the accuracy of using the approximating ODE. In the final chapter we find that when the fluid's power-law index is in the range $0.4 \leq n \leq 1$, an appropriate method of solving the approximating ODE yields solutions whose relative errors are less than 1%. However, this relative error increases with decreasing values of n so that in the range $0 \leq n < 0.4$ it reaches a maximum value of approximately 6%. Thus, at least for values of $0.4 \leq n \leq 1$ the approximating ODE presents an accurate and computationally fast alternative to solving the semi-infinite problem. The same can't be said for values of $0 \leq n < 0.4$, but the methods presented in this thesis may be used as a starting point for future work in this direction.

Preface

This dissertation is original, unpublished, independent work by the author, D. Gomez.

Table of Contents

List of Figures

Acknowledgements

I want to thank my supervisors Dr. Anthony Peirce and Dr. Michael Ward for their guidance and support both inside and outside of the classroom. I would also like to thank Dr. Egor Dontsov, whose work with Dr. Peirce at UBC motivated much of the work in this thesis. Finally, I am grateful to NSERC for funding my first year in this program through a one-year NSERC CGS-M fellowship.

Chapter 1

Introduction

Since its inception and first implementation in the early 19th century [1], the method of hydraulic fracturing as a means of stimulating oil reserves has become ubiquitous in the oil and gas industry. Hydraulic fractures are best described as brittle fractures that propagate due to the injection of a highly viscous fluid. Outside of the oil and gas industry hydraulic fractures arise naturally as a central mechanism in the formation of kilometre long dikes for magma transport, or they are artificially induced for applications in mine caving operations or soil remediation projects (see [4] and the references therein). In each case the composition of propagating fluid and scale of the fractures may differ, but the phenomenon of hydraulic fracturing remains the same. The quantitative modelling of hydraulic fractures dates back to the late 1950s [1] and has been motivated both by naturally occurring phenomena, as well as by the prospect of better understanding and optimizing the use of hydraulic fracturing in industrial applications. The study of hydraulic fracturing as it pertains to the oil and gas industry has been of particular interest due to its wide use and its engineering, economic, and environmental implications. For this reason this thesis will focus primarily on the study of hydraulic fractures in the context of reservoir stimulation.

To motivate the need for quantitative models of hydraulic fractures it is instructive to first understand their role in the oil and gas industry. While oil may be extracted by conventional methods from a variety of reservoirs (e.g. sandstone formations), other low permeability rock formations, such as as shale, are not susceptible to conventional methods [5]. However, reservoir stimulation techniques have been developed which allow access to oil locked within these otherwise inaccessible reservoirs. In general reservoir stimulation projects share the following key steps. First a hole, known as a wellbore, is drilled into the ground to access deep underground oil reservoirs. After the wellbore has been established numerous explosive charges on the wellbore walls are discharged. This creates weak regions in the surrounding rock that serve as the starting location of the hydraulic fractures. Next, a highly viscous fluid is pumped into the wellbore at a high pressure, which results in the propagation of hydraulic fractures at each of the discharge sites. This is followed by pumping in a polymer mixture responsible for the "filter cake" building mechanism that mediates leak-off of the fracturing fluid into the surrounding rock. After the hydraulic fractures have reached a sufficient width, a proppant mixture is pumped into the fractures with the purpose of keeping them open while the fracturing fluid is removed. With the fracturing fluid removed, a negative pressure gradient drives the surrounding oil into the hydraulic fractures and up the wellbore for collection [1, 5].

With the above procedure in mind we can motivate the study of quantitative models of hydraulic fractures by considering two problems. The first is known as premature proppant bridging and it occurs when the proppant is pumped while the hydraulic fracture is not sufficiently wide. This creates a barrier that does not allow the proppant to adequately fill the hydraulic fracture thereby causing issues when the fracturing fluid is removed. Current technologies are unable to make fracture width measurements during a hydraulic fracturing treatment so having quantitative models that describe how the frac-

ture width evolves with time are crucial to prevent premature bridging. Another problem we can consider is that of fracture efficiency which is typically defined as the ratio of the volume of fluid stored in the fracture to the total volume pumped in. Ideally this ratio would equal one but due to fluid loss through leak-off it is typically smaller. A quantitative understanding of how the problem parameters affect this ratio is clearly of great importance both in terms of optimizing resource usage as well as reducing potentially negative environmental effects.

The highly complex nature of hydraulic fractures means that, with the exception of a few simplified scenarios, solutions are obtained almost exclusively by numerical methods. However, even to obtain a numerical solution there are still significant hurdles that must be overcome. The most notable challenges include moving boundaries as well as the multi-scale behaviour inherent in hydraulic fracture propagation. Fortunately, substantial progress can be made in addressing both these challenges by furthering our understanding of the hydraulic fracture's tip behaviour. Moreover it can be shown (see Appendix B of [19]) that near its tip, a hydraulic fracture behaves like a semi-infinite hydraulic fracture under plane strain conditions. In contrast to the general hydraulic fracturing problem, the semi-infinite case is more amenable to analytical techniques and has therefore been the focus of numerous studies. These studies typically involve finding asymptotic solutions in distinguished parameter regimes and using this to then calculate the full semi-infinite solution structure numerically as is done in [9, 10] for Newtonian fracturing fluids and [3, 15, 16] for power-law fluids.

One of the key difficulties in the numerical solution of the semi-infinite problem is the coupling between a singular integral equation and a non-linear ordinary differential equation. The recent work by Dontsov and Peirce [6] overcomes this difficulty by reformulating this problem in terms of a single non-singular and non-linear integral equation,

which is readily solved using standard numerical methods such as Simpson's rule and Newton's method. Moreover Dontsov and Peirce obtained an approximating separable ordinary differential equation from which they were able to obtain an approximating solution, which is both fast to calculate and is in excellent agreement with full numerical solutions of the semi-infinite problem. The most important feature of this approximation is the speed with which its solutions can be computed. Indeed, multiscale hydraulic fracture simulators require the rapid computation of the tip asymptotes in order to run in a reasonable time. Motivated by these results as well as those obtained by Adachi and Detournay [3] as well as Linkov [15, 16], the present thesis considers the non-singular reformulation of the problem governing semi-infinite hydraulic fractures driven by a power-law fluid. Furthermore, as was done by Dontsov and Peirce for Newtonian fluids, one of our primary goals is to obtain an approximate solution that is both fast to calculate and reliably captures the solution of the semi-infinite fracture. Future sections will demonstrate that we have partially succeeded in this goal by obtaining a solution that is fast to calculate but has a limited range of reliability.

The proceeding sections are organized in the following way. In Chapter 2 we will discuss the relevant mathematical modelling, making more precise the underlying assumptions of our simplified model. Chapter 3 discusses in detail the relevant scaling and resulting asymptotic regimes of propagation for hydraulic fractures driven by power-law fluids. In Chapter 4 we will extend the formulation of Dontsov and Peirce [6] to the power-law fluid case, and this is followed by a discussion of the approximating ODE and its solution structure in Chapter 5. Finally, before the concluding remarks of Chapter 7, in Chapter 6 we will discuss the numerical implementation of the reformulation from Chapter 4.

Chapter 2

Mathematical Model

As discussed in the previous chapter, our study of the semi-infinite hydraulic fracture problem is largely motivated by its connection and practical relevance to more general fracturing problems (see for example [4] and Appendix B of [19]). We therefore consider the case of a hydraulic fracture under plane strain conditions driven by a power-law fluid. The fracture is assumed to propagate in the positive X direction at a constant velocity V (see Figure 2.1) so that $X_{\text{tip}} = Vt$. The distance from the fracture tip as measured from within the fracture is denoted by x and is given by $x = X_{\text{tip}} - X$. Furthermore we assume that the fracture velocity is sufficiently slow so that elastic deformations depend solely on

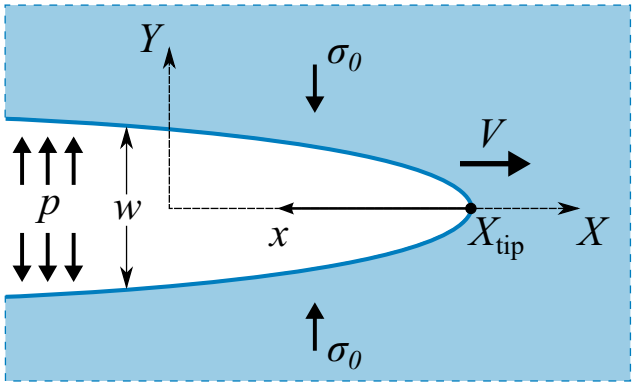

Figure 2.1: Geometry of a semi-infinite hydraulic fracture.

the distance from the fracture tip, x, and are otherwise independent of time. We make reference to the fixed coordinate X only when describing the behaviour of the fracturing fluid, which in the absence of fluid lag is also assumed to travel in the positive X direction at the same constant velocity V.

The modelling of hydraulic fractures involves the coupling of two sub-fields of continuum mechanics – elasticity theory and fluid mechanics. We are primarily interested in obtaining the fracture width $w(x)$ (or $w(X,t)$ in the fixed coordinates) from the modelling, but as we will soon see the fluid pressure $p_f(x)$ can be obtained as a by-product. To facilitate the modelling of hydraulic fractures, we can isolate four distinct but strongly coupled physical phenomena. From the point of view of elasticity this involves the singular behaviour of the stress field at the tip and the related criterion for propagation, as well as the coupling between the internal pressure of the fracture and the resulting elastic deformation. These two phenomena are discussed in the Elasticity Theory section below and involve the use of the stress function approach as well as ideas from dislocation theory. The remaining two phenomena involve the behaviour of the fluid, the first modelling the propagation of the fluid using lubrication theory, and the second modelling the loss of fluid by leak-off using Carter's leak-off model.

2.1 Elasticity Theory

We begin our discussion by exploring how the surrounding elastic material responds to hydraulic fractures. This interaction occurs via two mechanisms – the geometric disturbance caused by the fracture, and by interactions with the fracturing fluid. Both of these interactions are aptly described using ideas from elasticity theory. In particular the geometric effect is found to be concentrated at the fracture tip and can therefore be described using asymptotic approximations. Furthermore, as we will see the tip behaviour

is closely linked with the propagation criterion for the fracture by what is known as the stress intensity factor and the material toughness. Finally, using ideas from dislocation theory the interaction between the elastic material and the fracturing fluid leads to a relationship between the fluid pressure and the fracture width.

2.1.1 Tip Asymptotics and Propagation Criterion

To describe the tip asymptotics we follow the method of Williams [20] as set out in the excellent textbook on dislocations by Hills et. al. [12] by first considering the problem of a notch of angle 2φ within an infinite elastic material under plane strain conditions and with symmetric uni-axial remote loading (see Figure 2.2). Furthermore we assume that the notch is stationary (i.e. φ is fixed) and therefore satisfies the steady Navier equations. Such a notch asymptotically describes the opening of a fracture near its tip. We seek an Airy stress function $\mathfrak{U}$ defined by

$$\sigma_{\theta\theta} = \frac{\partial^2 \mathfrak{U}}{\partial r^2}, \qquad \sigma_{r\theta} = -\frac{\partial}{\partial r}\left(\frac{1}{r}\frac{\partial \mathfrak{U}}{\partial \theta}\right), \qquad \sigma_{rr} = \frac{1}{r^2}\frac{\partial^2 \mathfrak{U}}{\partial \theta^2} + \frac{1}{r}\frac{\partial \mathfrak{U}}{\partial r}. \tag{2.1}$$

Then the Airy stress function satisfies the biharmonic equation

$$\Delta^2 \mathfrak{U} \equiv \left(\frac{\partial^2}{\partial r^2} + \frac{1}{r}\frac{\partial}{\partial r} + \frac{1}{r^2}\frac{\partial^2}{\partial \theta^2}\right)^2 \mathfrak{U} = 0,$$

for which we seek a solution of the form $\mathfrak{U} = r^\lambda f(\theta)$. Note that with $\mathfrak{U}$ of this form $\sigma = O(r^{\lambda-2})$ and the displacement field is $u = O(r^{\lambda-1})$. We are interested in the dominant

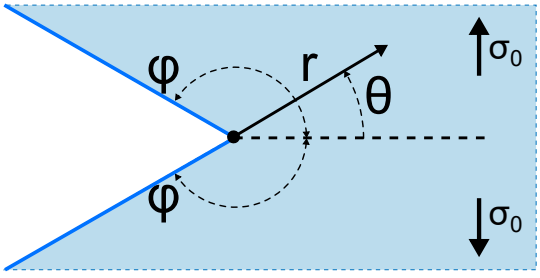

Figure 2.2: Infinite notch modelling the fracture tip.

behaviour for small r and therefore seek the smallest value of λ which, in order to ensure u remains finite, satisfies $\lambda > 1$. By defining $g(\theta) = f''(\theta) + \lambda^2 f(\theta)$ we find

$$g''(\theta) + (\lambda - 2)^2 g(\theta) = 0 \Longrightarrow g(\theta) = a\cos(\lambda - 2)\theta + b\sin(\lambda - 2)\theta,$$

where a and b are arbitrary constants. By symmetry of the loading we expect $\mathfrak{U}$ to be symmetric and therefore set $b = 0$. Thus

$$f''(\theta) + \lambda^2 f(\theta) + a\cos(\lambda - 2)\theta \Longrightarrow f(\theta) = A\cos\lambda\theta + B\cos(\lambda - 2)\theta,$$

where $B = \frac{a}{4(\lambda - 1)}$ is an arbitrary constant and we have again used symmetry to remove the sinusoidal solution $\sin\lambda\theta$. Now, since the notch is stationary we impose the traction free boundary conditions $\sigma_{r\theta} = \sigma_{\theta\theta} = 0$ at $\theta = \pm\varphi$ (by symmetry we only need to consider one angle, say $\theta = \varphi$) which yields the homogeneous system of equations

$$\begin{aligned} A\lambda(\lambda - 1)\sin\lambda\varphi + B(\lambda - 1)(\lambda - 2)\sin(\lambda - 2)\varphi = 0, \\ A\lambda(\lambda - 1)\cos\lambda\varphi + B\lambda(\lambda - 1)\cos(\lambda - 2)\varphi = 0. \end{aligned} \tag{2.2}$$

Assuming $\lambda \neq 0, 1$ we deduce that for this system to have a non trivial solution it's determinant must vanish, which yields

$$\sin 2(\lambda - 1)\varphi + (\lambda - 1)\sin 2\varphi = 0.$$

The solution $\lambda = \lambda(\varphi)$ is shown in Figure 2.3 where we have chosen the range $\frac{\pi}{2} < \varphi < \pi$ with the intention of describing the fracture opening by the wedge. This figure reveals that the smallest value taken by $\lambda > 1$ is $\lambda = 3/2$ which occurs at $\varphi = \pi$. This results in $\sigma = O(r^{-1/2})$ which signifies a singularity in the stress field as the apex of the notch is approached. Note that the next solution at $\varphi = \pi$ is $\lambda = 5/2$ which gives the correction term for $\mathfrak{U}$ and consequently for the stress and displacement fields.

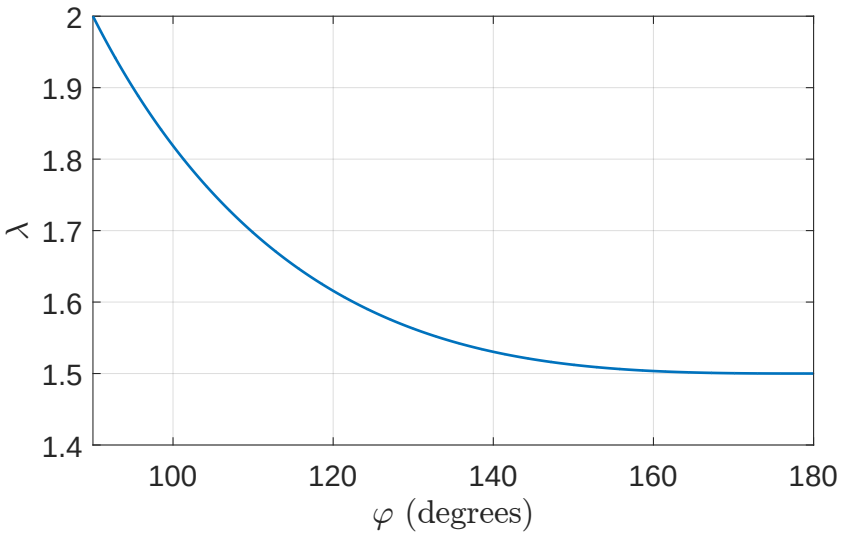

Figure 2.3: Plot of λ versus opening half-angle φ.

With $\varphi = \pi$ and $\lambda = 3/2$ we find that $\mathfrak{U} = r^{3/2}(A\cos\frac{3}{2}\theta + B\cos\frac{1}{2}\theta)$ and using (2.1) we deduce

$$\sigma_{r\theta} = \frac{K_I}{\sqrt{2\pi r}}\left(\frac{1}{4}\sin\frac{\theta}{2} + \frac{1}{4}\sin\frac{3\theta}{2}\right), \tag{2.3}$$

$$\sigma_{rr} = \frac{K_I}{\sqrt{2\pi r}}\left(\frac{5}{4}\cos\frac{\theta}{2} - \frac{1}{4}\cos\frac{3\theta}{2}\right), \tag{2.4}$$

$$\sigma_{\theta\theta} = \frac{K_I}{\sqrt{2\pi r}}\left(\frac{3}{4}\cos\frac{\theta}{2} + \frac{1}{4}\cos\frac{3\theta}{2}\right), \tag{2.5}$$

where $K_I = 3\sqrt{2\pi}A$ is known as the mode-I stress intensity factor. The square root singularity present in the stress field is ubiquitous in two-dimensional fracture problems. In particular the same singularity arises for both mode II and III fractures, which result in the definition of stress intensity factors K_{II} and K_{III} respectively (see Hills et. al. [12] for a detailed description).

We now turn to the question of the propagation criterion. The stress field formulae (2.3)-(2.5) reveal that regardless of the fracture geometry, there will be a square root singularity at the tip. However, not all fractures propagate, which suggests that it is the

strength of the singularity, characterized by K_I, that determines whether a fracture will propagate. Indeed Griffith proposed that a fracture propagates only when the energy released by the fracture exceeds that required to create two new surfaces [11]. This criterion takes the form [12]

$$G \geq 2\gamma, \tag{2.6}$$

where G is the energy release rate per unit area of the crack whereas 2γ represents the energy required to create two new surfaces. Furthermore the energy release rate is related to the stress intensity factor via [12]

$$G = \frac{4(1-\nu)}{8\mu} K_I^2,$$

whence we deduce that a fracture propagates only when the stress intensity factor exceeds some value K_{Ic} known as the material toughness.

Assuming the fracture is slowly propagating, we replace K_I with K_{IC} in (2.3)-(2.5) whence a lengthy calculation yields the displacement field

$$u_x(r,\theta) = \frac{K_{Ic}}{2\mu}\sqrt{\frac{r}{2\pi}}\cos\frac{\theta}{2}\left(3-4\nu-\cos\theta\right), \quad u_y(r,\theta) = \frac{K_{Ic}}{2\pi}\sqrt{\frac{r}{2\pi}}\sin\frac{\theta}{2}\left(3-4\nu-\cos\theta\right), \tag{2.7}$$

where μ is the shear modulus and ν is Poisson's ratio. The fracture opening width $w(x)$ is related to the displacement $u_y(r,\theta)$ by $w(x) = u_y(x,\pi) - u_y(x,-\pi)$ where x is the distance from the tip. Thus, both the propagation criterion and the near field behaviour of the fracture opening can be encoded in the single equation

$$w(x) \sim \frac{8}{\sqrt{2\pi}}\frac{K_{Ic}}{E'}x^{1/2} + O(x^{3/2}) \qquad (x \to 0^+), \tag{2.8}$$

where $E' = \frac{E}{1-\nu^2}$ and we have used that in plane strain the shear stress and Young's modulus are related by $E = 2(1+\nu)\mu$.

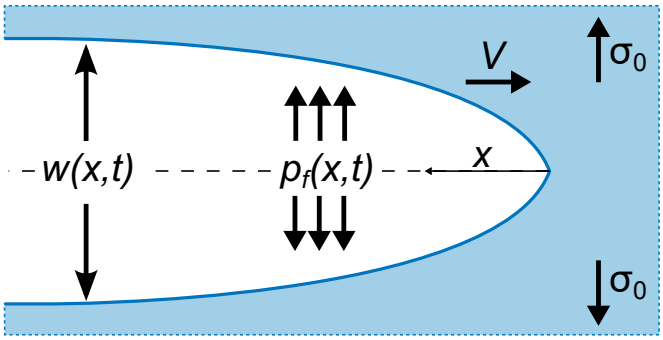

Figure 2.4: Schematic of propagating hydraulic fracture.

2.1.2 Dislocation Theory

We focus now on the interaction between the elastic material and the fracturing fluid. As depicted in Figure 2.4 we expect the fracturing fluid pressure p_f to exert outward forces on the fracture walls, driving the fracture ever wider and therefore increasing the width w. In this section we will be seeking a quantitative formulation of this interaction.

The first step is to determine the effect of a fracture on the elastic material's stress field. This is done by first considering the effect on the stress field due to a single edge dislocation. We will keep our discussion of dislocations brief and limited in generality, taking only what we need for subsequent sections. Some excellent resources on the theory of dislocations include the Book by Hills, et. al. [12] as well as the collection of papers edited by Mura [17] and in particular the papers by Hirth [13], Mura [18], and Dundurs [7] found therein. An edge dislocation represents a defect within an elastic material that results in a jump discontinuity $\mathbf{b}$ in the displacement field $\mathbf{u}$ as a clockwise path is followed about the dislocation core (see Figure 2.5a). We remark that the quantity $\mathbf{b}$ is known as the Burger's vector. We consider an edge dislocation centred at the origin with Burger's vector $(0, b_y)$ and such that there is a jump discontinuity in the y-component of the displacement field as the positive real axis is crossed (see Figure 2.5b). With the "+" and "−" symbols in

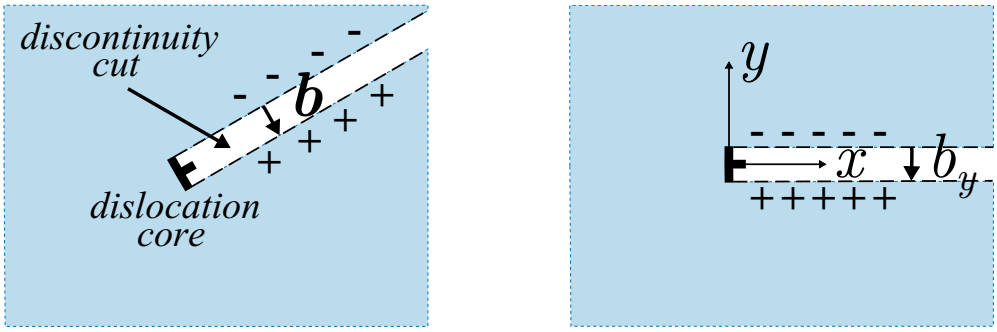

(a) Arbitrary edge dislocation with burgers vector **b**.

(b) Edge dislocation with cut along positive x axis and burgers vector $\mathbf{b} = (0, b_y)$.

Figure 2.5: Edge dislocation schematic.

Figure 2.5b imposing an orientation, the jump in the displacement is $u_y(+) - u_y(-) = b_y$ (note that the Burgers vector points downwards). Seeking a stress function that gives this jump discontinuity in the displacement field we obtain the stress field [12]

$$\sigma_{yy}(x) = \frac{E'}{4\pi}\frac{b_y}{x}. \tag{2.9}$$

Having found the response to a single dislocation we now consider a distribution of infinitesimal dislocations, each centred at $\xi \geq 0$ and having burgers vector $\delta b_y(\xi)$. Introducing the dislocation density $B_y(\xi)$ by defining $\delta b_y(\xi) = B_y(\xi)\, d\xi$ we now use (2.9) to obtain the stress field's response to each infinitesimal dislocation

$$\delta\sigma_{yy}(x;\xi) = \frac{E'}{4\pi}\frac{B_y(\xi)}{x-\xi}d\xi.$$

Integrating over all dislocations we obtain the total response

$$\sigma_{yy}(x) = \frac{E'}{4\pi}\fint_0^\infty \frac{B_y(\xi)}{x-\xi}d\xi, \tag{2.10}$$

where $\fint$ is the Cauchy Principal value.

It remains to determine the dependence of (2.10) on w. This is done by observing that every infinitesimal dislocation centred at $\xi < x$ contributes an amount $-B_y(\xi)d\xi$ to

the total jump discontinuity in the y-displacement at x and hence

$$w(x) = -\int_0^x B_y(\xi)d\xi \Longleftrightarrow B_y(x) = -\frac{\mathrm{d}w}{\mathrm{d}x},$$

whence (2.10) becomes

$$\sigma_{yy} = -\frac{E'}{4\pi}\int_0^\infty \frac{\partial w}{\partial \xi}(\xi, t)\frac{d\xi}{x-\xi}.$$

Finally we relate the stress field to the pressure $p(x,t) = p_f(x,t) - \sigma_0$ by noting that the stress field on the boundary σ_{yy} calculated above is related to $p(x,t)$ via $p(x,t) = -\sigma_{yy}(x,t)$ and hence

$$p(x,t) = \frac{E'}{4\pi}\int_0^\infty \frac{\partial w}{\partial \xi}(\xi, t)\frac{ds}{x-s}\,ds \tag{2.11}$$

2.2 Fluid Mechanics

Having established the elastic material's response to the hydraulic fracture, we now explore the behaviour of the propagating fluid within the hydraulic fracture. This is accomplished in three parts. First we determine the appropriate form of Poiseuille's law for a power-law fluid, which relates the pressure gradient to the fluid flux. Secondly we discuss Carter's leak-off model, which describes how some of the fluid escapes the hydraulic fracture and enters the elastic material. Finally the resulting equations from these two discussions are combined by considering mass-conservation which leads to the governing equation for the propagating fluid. Throughout this section we will begin by considering the fracturing fluid in a fixed reference frame with the X-Y axes oriented in such a way that the fracture propagates along the positive X direction and is centred on the Y axis (see Figure 2.1). After establishing the relevant equations we reintroduce the distance from the tip x by changing to the moving coordinates $x = VT - X$.

2.2.1 Poiseuille's Law for Power-Law Fluids

Our leading assumptions for the hydraulic fracture and the fluid it confines are that the fluid moves sufficiently slowly that the inertial forces are negligible in comparison to the viscous forces, the confining fracture is much longer than it is wide, the fluid's velocity is restricted to the $X-Y$ plane, and the fluid satisfies a no-slip boundary condition along the fracture walls (i.e. along $Y=\pm w/2$). In light of these assumptions, the formulation of lubrication theory applies. The derivation leading to Poiseuille's law is standard, and for this reason we omit many of the details, pointing out only those areas where the power-law rheology of the fluid plays a critical rule. We recall that the power-law rheology takes the form

$$\tau_{ij} = M(2\dot{\varepsilon}_{ij})^n = M\left(\frac{\partial V_i}{\partial X_j} + \frac{\partial V_j}{\partial X_i}\right)^n, \tag{2.12}$$

where n is the power-law index, M the consistency index, and V_i the components of the velocity field. We restrict the power-law index to $0 < n \leq 1$, which reflects the shear-thinning rheology of fluids typically used in reservoir stimulation projects [8]. In addition to assuming the fluid is laminar we also assume that the confining fracture is much longer than it is wide. The fluid therefore satisfies the conditions of lubrication theory, which leads to the following relationship between the pressure gradient and the X-component of the velocity

$$\frac{\partial p}{\partial X} = nM\left(\frac{\partial V_X}{\partial Y}\right)^{n-1}\frac{\partial^2 V_X}{\partial Y^2}, \qquad \text{in} \quad -\frac{w}{2} < Y < \frac{w}{2}; \qquad v = 0, \qquad \text{on} \quad Y = \pm\frac{w}{2}.$$

Using symmetry to eliminate the constant resulting from the first integration, and then integrating again yields the velocity profile

$$V_X(X,Y,t) = -\frac{n}{n+1}\left(\frac{1}{M}\left|\frac{\partial p}{\partial X}\right|\right)^{1/n}\left(|Y|^{\frac{n+1}{n}} - \left(\frac{w}{2}\right)^{\frac{n+1}{n}}\right).$$

Integrating the velocity profile from $Y = -w/2$ to $+w/2$ yields the fluid flow rate

$$q(X,t) \equiv \int_{-w/2}^{w/2} V(X,Y,t)\, dy = \left(\frac{1}{M'}\left|\frac{\partial p}{\partial X}\right|\right)^{1/n} w^{\frac{2n+1}{n}},$$

where

$$M' \equiv 2^{n+1}\left(\frac{2n+1}{n}\right)^{n} M. \tag{2.13}$$

Finally, we use the fact that $\partial p/\partial X < 0$ and $q > 0$ to solve for the pressure gradient, thereby obtaining Poseuille's law for a power-law fluid

$$\frac{\partial p}{\partial X} = -\frac{M' q^n}{w^{2n+1}}. \tag{2.14}$$

2.2.2 Carter's Leak-Off Model

The remaining phenomenon to be described is that of fluid leak-off. This phenomenon is described by Carter's leak-off model as follows. First, as the fluid leaks some of it is deposited in a region immediately surrounding the fracture making up what is known as the filter cake. The fluid that makes it past the filter cake is known as the filtrate and the region it propagates in is known as the invaded zone. Beyond the invaded zone we assume that the elastic material is naturally saturated with a reservoir fluid, thereby putting up a pressure barrier which resists the filtrate fluid. With this process in mind, the leading assumptions of Carter's leak-off are that (1) the leak-off fluid flows perpendicular to the fracture boundary thereby rendering it a one-dimensional process, (2) the reservoir pressure p_r is much larger than the fluid pressure p_f, (3) the rate at which the filter cake grows is directly proportional to the the amount of fluid passing through it, and (4) the leaking fluid satisfies Darcy's law in both the invaded zone and the filter cake. In addition to these four assumptions, we add a fifth which addresses the power-law behaviour of the fracturing fluid and states that (5) the added polymers that gives the fracturing fluid it's power-law rheology are used up to build the filter cake and therefore do not otherwise

contribute to the leak-off process. This final assumption effectively allows us to treat the leaking fluid as a Newtonian fluid which greatly simplifies the resulting leak-off term and moreover allows us to keep the same leak-off term found in the hydraulic fracturing literature.

With the fifth assumption in mind we refer to the excellent exposition of Carter's leak-off model found in Adachi's Ph.D. thesis [2, p.18-23] which leads to the expression

$$g(X,t) = \frac{2C_L}{\sqrt{t - t_0(X,t)}}, \qquad t > t_0(X,t), \tag{2.15}$$

where C_L is Carter's leak-off coefficient and $t - t_0$ represents the elapsed time since the fracture tip first passed the point currently at a distance x away from the fracture tip. We remark here that the paper by Linkov [16] considers the problem of a hydraulic fracture with a more general leak-off term of the form

$$g(X,t) = \frac{2C_L}{[t - t_0(X,t)]^{\beta}}.$$

Furthermore, by reproducing the derivation found in [2] but using the power-law rheology, it can be shown that $\beta = \frac{1}{n+1}$, though the utility of this added generality is lost in view of the fifth assumption.

2.2.3 Mass Conservation and The Lubrication Equation

The continuity equation for the fracturing fluid including leak-off takes the form

$$\frac{\partial w}{\partial t} + \frac{\partial q}{\partial X} + g = 0. \tag{2.16}$$

Changing to the moving coordinate $x = Vt - X$ we obtain

$$\frac{\partial}{\partial t} = V\frac{\mathrm{d}}{\mathrm{d}x}, \qquad \frac{\partial}{\partial X} = -\frac{\mathrm{d}}{\mathrm{d}x},$$

Variable	x	w	p	E'	V	C'	M'	K'
Units	$\mathfrak{L}$	$\mathfrak{L}$	$\mathfrak{F}\mathfrak{L}^{-2}$	$\mathfrak{F}\mathfrak{L}^{-2}$	$\mathfrak{L}\mathfrak{T}^{-1}$	$\mathfrak{L}\mathfrak{T}^{-1/2}$	$\mathfrak{F}\mathfrak{T}^{n}\mathfrak{L}^{-2}$	$\mathfrak{F}\mathfrak{L}^{-3/2}$

Table 2.1: Units of problem variables and parameters ($\mathfrak{L}$ = length, $\mathfrak{T}$ = time, $\mathfrak{F}$ = force).

and moreover the elapsed time $t - t_0(X,t)$ in Carter's leak-off model (2.15) is easily seen to equal x/V whence the continuity equation becomes

$$V\frac{\mathrm{d}w}{\mathrm{d}x} - \frac{\mathrm{d}q}{\mathrm{d}x} + \frac{2C_L V^{1/2}}{\sqrt{x}} = 0.$$

Integrating and substituting (2.14) in for q we obtain

$$Vw - \left(\frac{w^{2n+1}}{M'}\frac{\mathrm{d}p}{\mathrm{d}x}\right)^{1/n} + 4C_L V^{1/2}x^{1/2} = 0,$$

from which we readily obtain the lubrication equation

$$\frac{\mathrm{d}p}{\mathrm{d}x} = \frac{M'V^n}{w^{n+1}}\left(1 + \frac{4C_L}{V^{1/2}}\frac{x^{1/2}}{w}\right)^n. \tag{2.17}$$

2.3 Summary of Governing Equations

We conclude this section by summarizing the governing equation and relevant parameter definitions. For convenience, we introduce the parameters

$$M' \equiv 2^{n+1}\left(\frac{2n+1}{n}\right)^n M, \qquad K' \equiv \frac{8}{\sqrt{2\pi}}K_{Ic}, \qquad C' \equiv 2C_L.$$

With these parameters the governing equations are summarized below.

Lubrication Equation:

$$\frac{\mathrm{d}p}{\mathrm{d}x} = \frac{M'V^n}{w^{n+1}}\left(1 + \frac{2C'}{V^{1/2}}\frac{x^{1/2}}{w}\right)^n. \tag{2.18}$$

Elasticity Equation:

$$p(x) = \frac{E'}{4\pi}\int_0^\infty \frac{\mathrm{d}w}{\mathrm{d}s}\frac{ds}{x-s}. \tag{2.19}$$

Fracture Tip Equation (with Propagation Criterion):

$$w(x) \sim \frac{K'}{E'} x^{1/2} + O(x^{3/2}) \qquad (x \to 0^+). \tag{2.20}$$

Finally the units of all problem parameters and variables are summarized in Table 2.1 above.

Chapter 3

Problem Scaling and Asymptotic Regimes

A ubiquitous step in the analysis of mathematical models is to non-dimensionalize its governing equations. This procedure has many benefits such as reducing the number of parameters and determining scale invariants of the underlying problem. In the context of hydraulic fractures non-dimensionalization yields another benefit – it leads to a substantial simplification of the governing equations in three distinct parameter regimes. In each of these parameter regimes the governing equations are simplified to an extent that closed-form solutions can be determined. Moreover, each regime can be associated with a distinct length scale thereby allowing us to associate each of the closed form solutions with the behaviour of the solution at a particular length scale. This final point is the most important for subsequent discussions. Although we will not use the scalings introduced in this chapter for subsequent ones, we will be making use of the behaviour of solutions when $x \ll 1$ and when $x \gg 1$.

Before proceeding with the non-dimensionalization it is instructive to keep track

of the units of each variable and parameter in our problem for which we refer the reader to Table 2.1. Next we introduce the dimensionless variables ξ, Ω, and Π defined by

$$\xi = x/l, \qquad \Omega = w/l, \qquad \Pi = p/E'.$$

Substituting this into the (rearranged) lubrication equation (2.18) and the tip constraint (2.20) we obtain

$$\frac{\mathrm{d}\Pi}{\mathrm{d}\xi} = \left(\frac{(M')^{\frac{1}{n}} V}{(E')^{\frac{1}{n}} l} \frac{1}{\Omega^{\frac{n+1}{n}}} + \frac{2(M')^{\frac{1}{n}} C' V^{1/2}}{(E')^{\frac{1}{n}} l^{3/2}} \frac{\xi^{1/2}}{\Omega^{\frac{2n+1}{n}}} \right)^n,$$
$$\Omega \sim \frac{K'}{E' l^{1/2}} \xi^{1/2} + O(\xi^{3/2}) \qquad (\xi \to 0^+).$$

We note that the scaling leaves the elasticity equation (2.19) invariant except for cancelling out the Young's modulus E'. In the above dimensionless equations we recognize three dimensionless groups

$$\mathcal{G}_m \equiv \frac{(M')^{\frac{1}{n}} V}{(E')^{\frac{1}{n}} l}, \qquad \mathcal{G}_k \equiv \frac{K'}{E' l^{1/2}}, \qquad \mathcal{G}_c \equiv \frac{2(M')^{\frac{1}{n}} C' V^{1/2}}{(E')^{\frac{1}{n}} l^{3/2}} = \frac{2\mathcal{G}_m C'}{V^{1/2} l^{1/2}}. \tag{3.1}$$

We make two observations. First the dimensionless groups $\mathcal{G}_m$ and $\mathcal{G}_k$ are directly proportional to M' and K' respectively. Second, we observe that the dimensionless group $\mathcal{G}_c$ is proportional not only to C' but also to $\mathcal{G}_m$ and therefore M'. This second observation is going to play an important role when we consider different scaling regimes since $\mathcal{G}_m = 0$ will always imply $\mathcal{G}_c = 0$. With these dimensionless groups defined as in (3.1) we obtain the dimensionless equations

$$\frac{\mathrm{d}\Pi}{\mathrm{d}\xi} = \left(\frac{\mathcal{G}_m}{\Omega^{\frac{n+1}{n}}} + \mathcal{G}_c \frac{\xi^{1/2}}{\Omega^{\frac{2n+1}{n}}} \right)^n \tag{3.2}$$

$$\Pi = \frac{1}{4\pi} \int_0^\infty \frac{\Omega'(\zeta)}{\xi - \zeta} \, d\zeta, \tag{3.3}$$

and

$$\Omega \sim \mathcal{G}_k \xi^{1/2} + O(\xi^{3/2}) \qquad (\xi \to 0^+). \tag{3.4}$$

At this stage we note that the length scale l remains undefined. This additional degree of freedom allows us to set one of the dimensionless groups appearing in (3.1) to unity and solve for l. Hence each parameter M', K', and C' is directly associated with a length scale. Individually setting one of $\mathcal{G}_m$, $\mathcal{G}_k$, and $\mathcal{G}_c$ to unity we therefore obtain the three distinct length scales given by

$$l_m = \frac{(M')^{\frac{1}{n}} V}{(E')^{\frac{1}{n}}}, \qquad l_k = \left(\frac{K'}{E'}\right)^2, \qquad l_c = \left(\frac{2(M')^{\frac{1}{n}} C' V^{1/2}}{(E')^{\frac{1}{n}}}\right)^{2/3}. \tag{3.5}$$

By setting one of the dimensionless groups in (3.1) to unity and the remaining ones to zero we can explore the behaviour of solutions when the propagation of the hydraulic fracture is dominated by one of three processes – viscosity (M), toughness (K), or leak-off (C). The remainder of this chapter explores the solution structure within each of these parameter regimes.

Before continuing to study each propagation regime we make note of the special collection of solutions to (3.3) for each $0 < \alpha < 1$ given by [14]

$$\Omega(\xi) = \beta \xi^{\alpha}, \qquad \Pi(\xi) = \delta \xi^{\alpha - 1}, \tag{3.6}$$

where

$$\delta = \frac{\alpha \beta}{4} \cot \pi\alpha. \tag{3.7}$$

3.1 Viscous Regime ($\mathcal{M}$)

In the viscous regime we have $\mathcal{G}_m = 1$, $\mathcal{G}_k = 0$, and $\mathcal{G}_c = 0$. The natural length scale is then given by $l = l_m$. We seek solutions of the form (3.6) whence the lubrication equation (3.2) yields

$$(\alpha - 1)\delta \xi^{\alpha - 2} = \frac{1}{\beta^{n+1} \xi^{(n+1)\alpha}}.$$

Collecting like powers of ξ we deduce that $\alpha = 2/(n+2)$ and then combining the resulting equation with (3.7) allows us to solve for β and δ. Summarizing the final result we have

$$\Omega_m \sim \beta_m \xi_m^{\alpha_m}, \qquad \Pi_m \sim \delta_m \xi_m^{\alpha_m - 1}, \tag{3.8}$$

where

$$\alpha_m = \frac{2}{n+2}, \qquad \beta_m = \left(\frac{-2(n+2)^2}{n\cot(\pi\alpha_m)}\right)^{\frac{1}{n+2}}, \qquad \delta_m = -\frac{n+2}{n}\beta_m^{-(n+1)}, \tag{3.9}$$

and where we have used a subscript m to emphasize the viscous scaling $l = l_m$.

3.2 Toughness Regime ($\mathcal{K}$)

For the toughness regime we have $\mathcal{G}_k = 1$, $\mathcal{G}_c = 0$, and $\mathcal{G}_m = 0$. In this case the natural length scale is then given by $l = l_k$. Seeking solutions of the form (3.6) satisfying (3.7), the tip behaviour (3.4) immediately implies that $\beta = 1$ and $\alpha = 1/2$. Then (3.7) implies that $\delta = 0$ so to leading order the solution pair in the toughness regime is given by

$$\Omega_{k0} = \xi^{1/2}, \qquad \Pi_{k0} = 0.$$

Assuming $\mathcal{G}_m, \mathcal{G}_c \ll 1$ we can deduce the leading order correction to Π by substituting $\Omega = \Omega_{k0}$ into the lubrication equation (3.2) which gives

$$\frac{\mathrm{d}\Pi_{k1}}{\mathrm{d}\xi} = (\mathcal{G}_m + \mathcal{G}_c)^n \xi^{-\frac{n+1}{2}}.$$

This equation is readily integrated, making special note of the logarithmic form of the solution when $n = 1$. Summarizing, when $\mathcal{G}_c$ and $\mathcal{G}_m$ are small, the leading order solution in the toughness regime is given by

$$\Omega_k \sim \xi_k^{1/2}, \qquad \Pi_k \sim \begin{cases} \frac{2}{1-n}(\mathcal{G}_m + \mathcal{G}_c)^n \xi_k^{\frac{1-n}{2}}, & n \neq 1, \\ (\mathcal{G}_m + \mathcal{G}_c)\log\xi_k, & n = 1, \end{cases} \qquad (\mathcal{G}_c, \mathcal{G}_m \ll 1), \tag{3.10}$$

where we've used the subscript k to remind the reader we are using the scaling $l = l_k$.

3.3 Leak-Off Regime ($\mathcal{C}$)

In the leak-off regime we set $\mathcal{G}_c = 1$ and use the length scale $l = l_c$. As alluded to earlier, since $\mathcal{G}_m = 0 \Longrightarrow \mathcal{G}_c = 0$, the present case requires that $\mathcal{G}_m \neq 0$ and we therefore can't proceed as in the previous two cases. Instead we proceed by setting $0 < \mathcal{G}_m \ll 1$ and $\mathcal{G}_k = 0$ and seeking a solution of the form

$$\Omega_c \sim \mathcal{G}_m^{\gamma}\Omega_{cm} + ..., \qquad \Pi_c \sim \mathcal{G}_m^{\gamma}\Pi_{cm} + ...,$$

where we have used the elasticity equation (3.3) to deduce the same power γ for the first order correction. In the absence of toughness the square-root asymptote predicted by the propagation criterion (3.4) no longer applies so we instead focus on the lubrication equation (3.2), which, to leading order, becomes

$$\mathcal{G}_m^{\gamma}\frac{\mathrm{d}\Pi_{cm}}{\mathrm{d}\xi} = \left(\mathcal{G}_m^{1-\gamma\frac{n+1}{n}}\frac{1}{\Omega_{cm}^{\frac{n+1}{n}}} + \mathcal{G}_m^{-\gamma\frac{2n+1}{n}}\frac{\xi^{1/2}}{\Omega_{cm}^{\frac{2n+1}{n}}}\right)^n. \tag{3.11}$$

The dominant balance in the small $\mathcal{G}_m$ is between the term on the left-hand-side and the second one on the right-hand-side which yields $\gamma = 0$ and the dominant equation

$$\Omega_{cm}^{2n+1}\frac{\mathrm{d}\Pi_{cm}}{\mathrm{d}\xi} = \xi^{n/2}.$$

Substituting a solution of the form (3.6) we immediately deduce the values of each parameter α, β, and δ whence we obtain the solution

$$\Omega_c \sim \beta_{cm}\xi_c^{\alpha_{cm}} + o(1), \qquad \Pi_c \sim \delta_{cm}\xi_c^{\alpha_{cm}-1} + o(1) \qquad (\mathcal{G}_m \ll 1), \tag{3.12}$$

where

$$\alpha_{cm} = \frac{n+4}{4(n+1)}, \qquad \beta_{cm} = \left(\frac{-64(n+1)^2}{3n(n+4)\cot(\pi\alpha_{cm})}\right)^{\frac{1}{2(n+1)}}, \tag{3.13}$$

and δ_{cm} is determined by using (3.7). We remark that, as in the previous two cases, we have used a subscript of c to remind the reader of the scaling $l = l_c$.

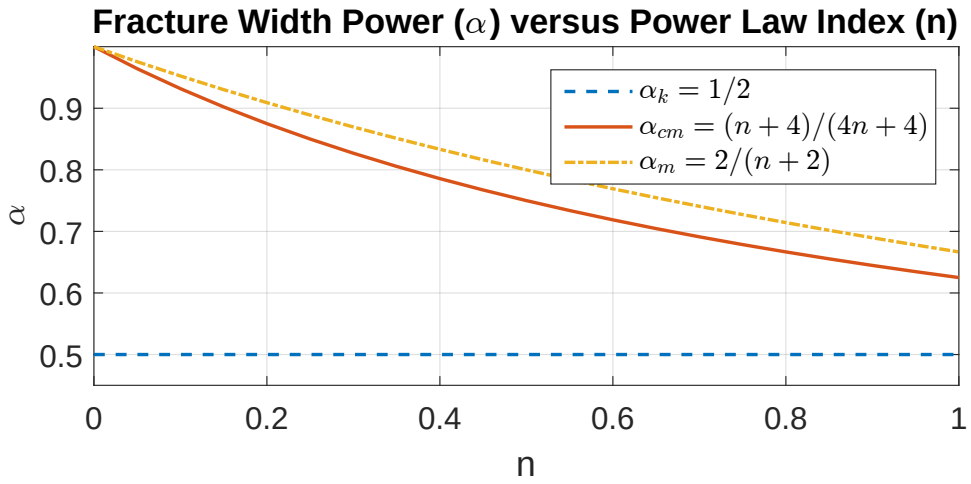

Figure 3.1: Fracture width power α in $\Omega \sim \beta\xi^{\alpha}$ for each parametric regime: α_k toughness, α_{cm} leak-off, and α_m viscous regime.

3.4 Comments on Negative Pressure

We begin by discussing the form of the dimensionless pressure within the viscosity and leak-off regimes. Since in each case $1/2 < \alpha < 1$ we deduce that $\cot(\pi\alpha) < 0$ and the pressure is therefore negative. This is best understood by considering the scenario of a dry semi-infinite fracture for which we have the classical solution $\Omega \propto \xi^{1/2}$ for the fracture opening [20, 12]. Within the viscosity and leak-off regimes the bound $\alpha > 1/2$ indicates that the fracture is narrower than in a dry fracture, meaning that the fluid is exerting a negative pressure along the opening boundaries [2].

3.5 Comment on the $n = 0$ Case

It is important to keep in mind that the $n = 0$ case does not represent a physically realistic system, and should rather be interpreted as a limiting solution for $n \to 0^+$. In this case the χ dependence vanishes from the governing equations, and as a result the leak-off regime also vanishes. The toughness solution remains unchanged. On the other

hand, ignoring the tip-asymptote we obtain the viscous solution $w = \sqrt{4\pi M'/E'}x$.

3.6 Spatial Ordering of Parameter Regimes

Analysing each parameter regime is not only instructive in understanding the solution structure in the three limiting cases, but it also allows us to determine the length scales at which each parameter regime dominates. In Figure 3.1 we observe the ordering

$$\alpha_k < \alpha_{cm} < \alpha_m, \qquad\qquad 0 < n \leq 1.$$

This suggests that for $\xi \ll 1$ the toughness ($\mathcal{K}$) regime will dominate, whereas for $\xi \gg 1$ the viscosity ($\mathcal{M}$) regime will dominate. Furthermore the leak-off regime ($\mathcal{C}$) regime dominates in some intermediate region. The resulting ordering is neatly summarized in the schematic of a fracture depicted in Figure 3.2.

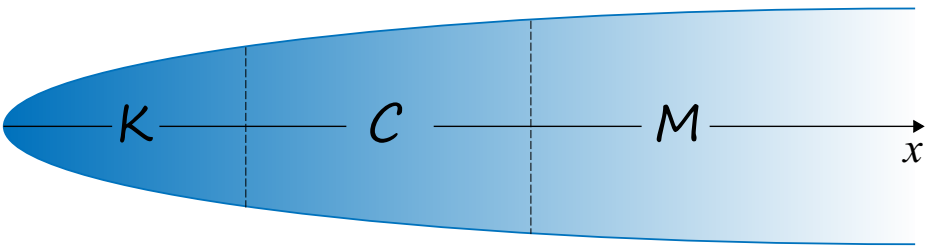

Figure 3.2: Schematic showing ordering of regions where each parameter regime dominates ($\mathcal{K}$: toughness, $\mathcal{C}$: leak-off, $\mathcal{M}$: viscosity).

Chapter 4

Non-Singular Integral Equation Formulation

Solutions to hydraulic fracture problems are typically obtained by simultaneously solving (2.18), (2.19), and (2.20) numerically. One of the biggest difficulties with this approach is dealing with the singular integral appearing in (2.19). Following the approach of Dontsov et. al. in [6] we will reformulate the current system of equations in the unknowns $w(x)$ and $p(x)$ as one non-singular and non-linear integral equation in the single unknown $w(x)$.

We proceed by inverting the elasticity equation (2.19) using the inversion formula found in [9]

$$w(x) = \frac{K'}{E'} x^{1/2} + \frac{4}{\pi E'} \int_0^\infty K(x,s) p(s)\, ds, \tag{4.1}$$

where the kernel $K(x,s)$ is given by

$$K(x,s) = \log\left|\frac{x^{1/2}+s^{1/2}}{x^{1/2}-s^{1/2}}\right| - 2\frac{x^{1/2}}{s^{1/2}}. \tag{4.2}$$

Observing that $K(x,s) = \frac{\partial F(x,s)}{\partial s}$ where

$$F(x,s) = (s-x)\log\left|\frac{x^{1/2}+s^{1/2}}{x^{1/2}-s^{1/2}}\right| - 2x^{1/2}s^{1/2}, \tag{4.3}$$

we may integrate the rightmost term in (4.1) by parts to get

$$\int_0^\infty K(x,s)p(s)\,ds = \lim_{s\to\infty} F(x,s)p(s) - \lim_{s\to 0^+} F(x,s)p(s) - \int_0^\infty F(x,s)p'(s)\,ds.$$

Provided we can evaluate the two limit terms resulting from the integration by parts, substituting the lubrication equation (2.18) in for $p'(s)$ will yield a non-linear integral equation in the single unknown function $w(x)$. We readily obtain

$$\begin{aligned} F(x,s) &\sim -4x^{1/2}s^{1/2} + O(s^{3/2}), && (s\to 0^+),\\ F(x,s) &\sim -\frac{4}{3}x^{3/2}s^{-1/2} + O(s^{-3/2}), && (s\to\infty). \end{aligned}$$

Furthermore, the parameter regime ordering determined in the previous chapter and more specifically the form of $\Pi(\xi)$ in (3.10) and (3.9) imply that

$$\begin{aligned} p(s) &\sim \begin{cases} O(s^{\frac{1-n}{2}}), & \text{if } n\neq 1,\\ O(\log s), & \text{if } n = 1, \end{cases} && (s\to 0^+),\\ p(s) &\sim O(s^{-\frac{n}{n+2}}), && (s\to\infty). \end{aligned}$$

Therefore both of the limits from the integration by parts vanish and after substituting the lubrication equation (2.18) in for $p'(s)$, the inverted elasticity equation (4.1) becomes

$$w(x) = \frac{K'}{E'}x^{1/2} + \frac{4M'V^n}{\pi E'}x^{1/2}\int_0^\infty \frac{s^{1/2}G(s^{1/2}/x^{1/2})}{w(s)^{n+1}}\left(1+\frac{2C'}{V^{1/2}}\frac{s^{1/2}}{w(s)}\right)^n ds, \tag{4.4}$$

where the kernel $G(t)$ is given by

$$G(t) = \frac{1-t^2}{t}\log\left|\frac{1+t}{1-t}\right| + 2. \tag{4.5}$$

We can further simplify (4.4) by introducing an appropriate scaling. Accordingly we introduce the non-dimensional variables $\tilde{w} = w/\hat{w}$ and $\tilde{x} = x/\hat{x}$ whence (4.4) becomes

$$\tilde{w}(\tilde{x}) = g_k\tilde{x}^{1/2} + \frac{4}{\pi}\tilde{x}^{1/2}\int_0^\infty \frac{\tilde{s}^{1/2}G(\tilde{s}^{1/2}/\tilde{x}^{1/2})}{\tilde{w}(\tilde{s})^{n+1}}\left(g_m + g_c\frac{\tilde{s}^{1/2}}{\tilde{w}(\tilde{s})}\right)^n \tilde{s},$$

where we have defined the non-dimensional groups

$$g_m \equiv \frac{(M')^{\frac{1}{n}} V \hat{x}^{\frac{2}{n}}}{(E')^{\frac{1}{n}} \hat{w}^{\frac{n+2}{n}}}, \qquad g_k \equiv \frac{K' \hat{x}^{1/2}}{E' \hat{w}}, \qquad g_c \equiv \frac{2(M')^{\frac{1}{n}} C' V^{\frac{1}{2}} \hat{x}^{\frac{n+4}{2n}}}{(E')^{\frac{1}{n}} \hat{w}^{\frac{2(n+1)}{n}}}. \tag{4.6}$$

Note that when $\hat{w} = \hat{x} = l$ each of these dimensionless groups reduce to the corresponding original dimensionless groups (3.1). Furthermore, from each dimensionless group we can determine a self-similar form for the solution on a different length scale. Indeed setting each dimensionless group g_k, g_c and g_m to unity we respectively obtain

$$\hat{w}_m = \left(\frac{M' V^n}{E'}\right)^{\frac{1}{n+2}} \hat{x}_m^{\frac{2}{n+2}}, \qquad \hat{w}_k = \frac{K'}{E'} \hat{x}_k^{1/2}, \qquad \hat{w}_c = \left(\frac{2^n M' (C')^n V^{\frac{n}{2}}}{E'}\right)^{\frac{1}{2(n+1)}} \hat{x}_c^{\frac{n+4}{4(n+1)}}.$$

Each such expression in turn suggests, respectively, the self-similar form

$$\tilde{w} = \frac{E'}{M' V^n} \frac{w^{n+2}}{x^2}, \qquad \tilde{w} = \frac{E'}{K'} \frac{w}{x^{1/2}}, \qquad \tilde{w} = \frac{E'}{2^n M' (C')^n V^{\frac{n}{2}}} \frac{w^{2(n+1)}}{x^{\frac{n+4}{2}}}.$$

Motivated by the analysis found in [6] we seek a solution of the form implied by the second self-similar form and therefore introduce the change of variables $\tilde{w} = \frac{E'}{K'} w / x^{1/2}$, $\tilde{x} = x^{1/2}/l^{1/2}$. The other two self-similar forms, while also valid, provide no significant simplification in the governing equations. Substituting this into (4.4) gives

$$\tilde{w}(\tilde{x}) = 1 + \frac{8}{\pi} \frac{M' V^n (E')^{n+1}}{(K')^{n+2}} l^{\frac{2-n}{2}} \int_0^\infty \frac{G(\tilde{s}/\tilde{x})}{\tilde{s}^{n-1} \tilde{w}(\tilde{s})^{n+1}} \left(1 + \frac{2C'E'}{V^{1/2} K'} \frac{1}{\tilde{w}(\tilde{s})}\right)^n d\tilde{s},$$

within which we can choose l and χ to reduce the number of parameters. Summarizing the results, we introduce new dimensionless variables $\tilde{w}$ and $\tilde{x}$ as well as a dimensionless parameter χ defined by

$$\tilde{w} = \frac{E'}{K'} \frac{w}{x^{1/2}}, \qquad \tilde{x} = \frac{x^{1/2}}{l^{1/2}}, \qquad l \equiv \left[\frac{(K')^{n+2}}{M' V^n (E')^{n+1}}\right]^{\frac{2}{2-n}}, \qquad \chi \equiv \frac{2C'E'}{V^{1/2} K'}, \tag{4.7}$$

so that (4.1) becomes

$$\tilde{w}(\tilde{x}) = 1 + \frac{8}{\pi} \int_0^\infty \frac{G(\tilde{s}/\tilde{x}) \tilde{s}^{1-n}}{\tilde{w}(\tilde{s})^{1+n}} \left(1 + \frac{\chi}{\tilde{w}(\tilde{s})}\right)^n d\tilde{s}. \tag{4.8}$$

Moreover with this scaling the propagation criterion (2.20) becomes $\tilde{w}(0) = 1$. This non-singular and non-linear integral equation will be the focus of the remaining discussions. In particular we will discuss how to obtain a first order ODE approximating (4.8), followed by brief discussion of the numerical solution to this ODE as well as some special cases for which an exact solution can be found.

4.1 Recovering Asymptotic Regimes from the Non-Singular Integral Equation

In this section we demonstrate that the solutions in each parameter regime obtained in Chapter 3 can be recovered directly from the non-singular integral equation (4.8). That this is the case for the toughness regime is immediately clear from the scaling (4.7) and the fact that $\tilde{w}(0) = 1$. To deduce the remaining asymptotic solutions we will make use of the identity (see Appendix A.1)

$$\int_0^\infty \frac{G(t)}{t^\alpha}\,dt = \frac{2\pi}{\alpha(2-\alpha)}\tan\left(\frac{\pi\alpha}{2}\right), \qquad (-1 < \alpha < 1). \tag{4.9}$$

We consider first the case of $\tilde{w} \gg \chi$. Then the integral equation (4.8) becomes

$$\tilde{w}(\tilde{x}) \sim \frac{8}{\pi}\int_0^\infty \frac{G(\tilde{s}/\tilde{x})\tilde{s}^{1-n}}{\tilde{w}(\tilde{s})^{1+n}}\,d\tilde{s}.$$

Seeking a monomial solution (reminiscent of the solution pairs used in 3) of the form $\tilde{w}(\tilde{x}) = \tilde{\beta}\tilde{x}^{\tilde{\alpha}}$ and using (4.9) we deduce

$$\tilde{\alpha} = \frac{2-n}{2+n}, \qquad \tilde{\beta} = \left[-\frac{2(2+n)^2}{n}\tan\left(\frac{2\pi}{2+n}\right)\right]^{\frac{1}{2+n}} = \beta_m. \tag{4.10}$$

After reversing the scaling (4.7) we find that this solution corresponds to the viscous solution described by (3.8) and (3.9).

Next we consider the case of $\tilde{w} \ll \chi$ so that, similarly to the the previous case, the integral equation (4.8) becomes

$$\tilde{w}(\tilde{x}) \sim \frac{8}{\pi}\chi^n \int_0^\infty \frac{G(\tilde{s}/\tilde{x})\tilde{s}^{1-n}}{\tilde{w}(\tilde{s})^{1+2n}}\, d\tilde{s}.$$

This time the monomial solution $\tilde{w}(\tilde{x}) = \tilde{\beta}\tilde{x}^{\tilde{\alpha}}$ yields

$$\tilde{\alpha} = \frac{2-n}{2(1+n)}, \qquad \tilde{\beta} = \left[-\frac{64(1+n)^2}{3n(4+n)}\tan\left(\frac{\pi(4+n)}{4(1+n)}\right)\right]^{\frac{1}{2(1+n)}} \chi^{\frac{n}{2(1+n)}} = \beta_{cm}\chi^{\frac{n}{2(1+n)}}, \tag{4.11}$$

which we can once again equate to the leak-off solution given by (3.12) and (3.13).

Chapter 5

Reduction to an Approximating First-Order ODE

In this chapter we will follow the procedure set out by Dontsov and Peirce in [6] to construct an ODE that approximates solutions to the non-singular integral equation (4.8). As briefly mentioned in the introduction, we are motivated to seek an approximate solution in order to cut down on computation time. While we may solve the full equation (4.8) numerically, the time required to do so results in multiscale hydraulic fracture simulators that are impractical. We will consider the cases $0 < n \leq 1$ and $n = 0$ separately, starting with the former. The resulting approximating ODE will be seemingly more complicated than the original non-linear integral equation, but we will be able to successively construct explicit solutions for it of the form $\tilde{x} = \tilde{x}(\tilde{w})$ where $\tilde{x}(\tilde{w})$ will be given by an integral that is fast to calculate using standard quadrature rules.

The key feature of the non-singular integral equation (4.8) that will allow us to approximate it by an ODE is the sharp transition from 4 to 1 that $G(t)$ undergoes near $t = 1$ on a logarithmic scale (see left pane of Figure 5.1). This suggests that $G'(t)$ will

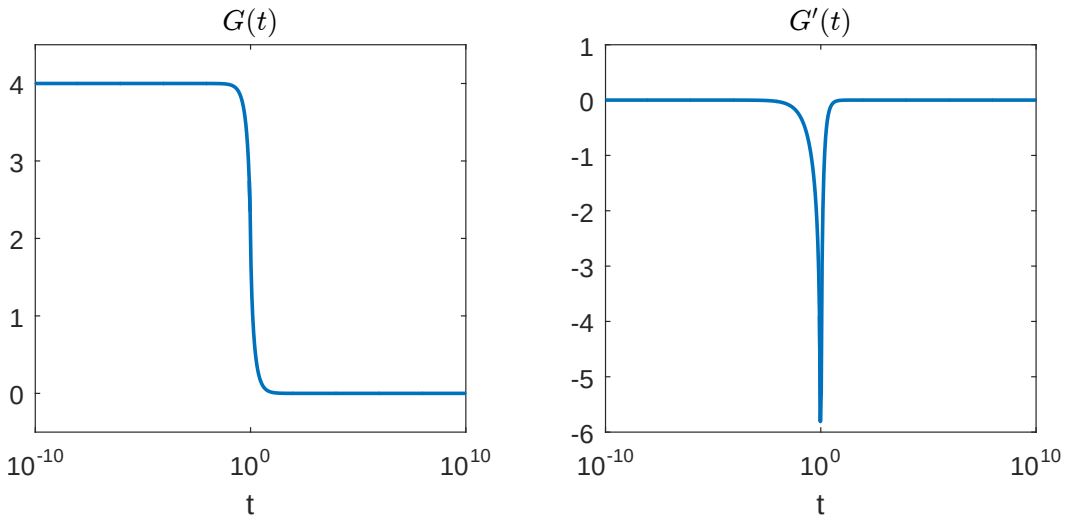

Figure 5.1: Plots of kernel function $G(t)$ and its first derivative $G'(t)$.

have a sharp peak near $t = 1$ on a logarithmic scale. Indeed, differentiating we obtain

$$G'(t) = -\frac{1+t^2}{t^2}\log\left|\frac{1+t}{1-t}\right| + \frac{2}{t}, \tag{5.1}$$

which is plotted in the right pane of Figure 5.1 and reveals a sharp peak at $t = 1$. Thus, if $f(t)$ varies slower than $G'(t)$ near $t = 1$, then the preceding discussion motivates the approximation

$$\int_0^\infty G'(t)f(t)g(t)\,dt \approx f(1)\int_0^\infty G'(t)g(t)\,dt, \tag{5.2}$$

where $g(t)$ is any function for which the integral on the right exists.

Returning to the construction of an approximating ODE, we begin by differentiating both sides of (4.8) and rearranging terms to obtain

$$\frac{\mathrm{d}\tilde{w}}{\mathrm{d}\tilde{x}} = -\frac{8}{\pi\tilde{x}^2}\int_0^\infty \frac{G'(\tilde{s}/\tilde{x})}{(1+\chi/\tilde{w}(\tilde{s}))^{1-n}}\frac{\tilde{s}^{2-n}}{\tilde{w}(\tilde{s})^{1+n}}\,d\tilde{s} - \frac{8\chi}{\pi\tilde{x}^2}\int_0^\infty \frac{G'(\tilde{s}/\tilde{x})}{(1+\chi/\tilde{w}(\tilde{s}))^{1-n}}\frac{\tilde{s}^{2-n}}{\tilde{w}(\tilde{s})^{2+n}}\,d\tilde{s}. \tag{5.3}$$

Similarly to the discussion in §4.1 we deduce that when $\tilde{w} \gg \chi$, the first term on the right-hand-side will dominate, whereas when $\tilde{w} \ll \chi$ it is the second term that dominates. Restricting first our attention to those value of $\tilde{x}$ where $\tilde{w}(\tilde{x}) \gg \chi$, the sharp peak of $G'(t)$

at $t = 1$ implies that the dominant contribution to the first integral on the right-hand-side will come from $\tilde{s} \approx \tilde{x}$ whence within that integral $\tilde{w}(\tilde{s}) \gg \chi$. Hence by the discussion in §4.1 we will have $\tilde{w}(\tilde{s}) = \tilde{\beta}\tilde{s}^{\tilde{\delta}}$ where $\tilde{\beta}$ and $\tilde{\delta}$ are both functions of $\tilde{s}$ that don't vary significantly from the corresponding values found in (4.10). In particular, quantities of the form $\frac{\tilde{w}(\tilde{s})}{(\tilde{s}/\tilde{x})^{\tilde{\delta}}}$ will not vary significantly for $\tilde{s} \approx \tilde{x}$. In addition since $(1 + \chi/\tilde{w}(\tilde{s})) \approx 1$ we can use (5.2) to obtain the following approximation

$$\begin{aligned}\int_0^\infty \frac{G'(\tilde{s}/\tilde{x})}{(1+\chi/\tilde{w}(\tilde{s}))^{1-n}} \frac{\tilde{s}^{2-n}}{\tilde{w}(\tilde{s})^{1+n}} d\tilde{s} &\approx \frac{\tilde{x}^{2-n}}{(1+\chi/\tilde{w}(\tilde{x}))^{1-n}} \int_0^\infty \frac{G'(\tilde{s}/\tilde{x})}{(\tilde{s}/\tilde{x})^{n-2+(1+n)\tilde{\delta}}} \left[\frac{(\tilde{s}/\tilde{x})^{\tilde{\delta}}}{\tilde{w}(\tilde{s})}\right]^{1+n} d\tilde{s} \\ &\approx \frac{\tilde{x}^{3-n}/\tilde{w}(\tilde{x})^{1+n}}{(1+\chi/\tilde{w}(\tilde{x}))^{1-n}} \int_0^\infty \frac{G'(t)}{t^{n-2+(1+n)\tilde{\delta}}} dt.\end{aligned} \tag{5.4}$$

To determine an appropriate approximation of the second integral appearing in (5.3) we proceed similarly. We restrict $\tilde{x}$ to the region where $\tilde{w}(\tilde{x}) \ll \chi$ and use the behaviour of $G'(t)$ to deduce that the dominant contribution in the second integral comes from $\tilde{s} \approx \tilde{x}$ where as a result $\tilde{w}(\tilde{s}) \ll \chi$. In contrast to the previous case we now have $(1 + \tilde{w}(\tilde{s})/\chi)^{1-n} \approx 1$ so the approximation becomes

$$\begin{aligned}\int_0^\infty \frac{G'(\tilde{s}/\tilde{x})}{(1+\chi/\tilde{w}(\tilde{s}))^{1-n}} \frac{\tilde{s}^{2-n}}{\tilde{w}(\tilde{s})^{2+n}} d\tilde{s} &\approx \frac{\chi^{n-1}\tilde{x}^{2-n}}{(1+\tilde{w}(\tilde{x})/\chi)^{1-n}} \int_0^\infty \frac{G'(\tilde{s}/\tilde{x})}{(\tilde{s}/\tilde{x})^{n-2+(1+2n)\tilde{\delta}}} \left[\frac{(\tilde{s}/\tilde{x})^{\tilde{\delta}}}{\tilde{w}(\tilde{s})}\right]^{1+2n} d\tilde{s} \\ &\approx \frac{\tilde{x}^{3-n}/\tilde{w}(\tilde{x})^{2+n}}{(1+\chi/\tilde{w}(\tilde{x}))^{1-n}} \int_0^\infty \frac{G'(t)}{t^{n-2+(1+2n)\tilde{\delta}}} dt.\end{aligned} \tag{5.5}$$

Combining (5.4) and (5.5) with (5.3) leads to the approximating ODE for $0 < n \leq 1$

$$\frac{\mathrm{d}\tilde{w}}{\mathrm{d}\tilde{x}} = \frac{C_1(\tilde{\delta}, n)}{(1+\chi/\tilde{w})^{1-n}} \frac{\tilde{x}^{1-n}}{\tilde{w}^{1+n}} + \chi \frac{C_2(\tilde{\delta}, n)}{(1+\chi/\tilde{w})^{1-n}} \frac{\tilde{x}^{1-n}}{\tilde{w}^{2+n}}, \qquad \tilde{w}(0) = 1, \tag{5.6}$$

where

$$C_1(\tilde{\delta}, n) \equiv -\frac{8}{\pi} \int_0^\infty \frac{G'(t)}{t^{n-2+(1+n)\tilde{\delta}}}\, dt, \tag{5.7}$$

$$C_2(\tilde{\delta}, n) \equiv -\frac{8}{\pi} \int_0^\infty \frac{G'(t)}{t^{n-2+(1+2n)\tilde{\delta}}}\, dt. \tag{5.8}$$

We proceed similarly for $n = 0$ with the added simplification that the problem is now independent of χ. We differentiate both sides of (4.8) when $n = 0$ to obtain

$$\frac{\mathrm{d}\tilde{w}}{\mathrm{d}\tilde{x}} = -\frac{8}{\pi\tilde{x}^2}\int_0^\infty G'(\tilde{s}/\tilde{x})\frac{\tilde{s}^2}{\tilde{w}(\tilde{s})}d\tilde{s}.$$

This time the approximation (5.2) takes the form

$$\begin{aligned}\int_0^\infty G'(\tilde{s}/\tilde{x})\frac{\tilde{s}^2}{\tilde{w}(\tilde{s})}d\tilde{s} &= \tilde{x}^2\int_0^\infty \frac{G'(\tilde{s}/\tilde{x})}{(\tilde{s}/\tilde{x})^{\tilde{\delta}-2}}\left[\frac{(\tilde{s}/\tilde{x})^{\tilde{\delta}}}{\tilde{w}(\tilde{s})}\right]d\tilde{s}\\ &\approx \frac{\tilde{x}^3}{\tilde{w}(\tilde{x})}\int_0^\infty \frac{G'(t)}{t^{\tilde{\delta}-2}}\,dt,\end{aligned}$$

where we have assumed the term in square brackets does not undergo a significant change near $\tilde{s} = \tilde{x}$. The resulting approximating ODE is therefore given by

$$\frac{\mathrm{d}\tilde{w}}{\mathrm{d}\tilde{x}} = C_0(\tilde{\delta})\frac{\tilde{x}}{\tilde{w}}, \qquad \tilde{w}(0) = 1, \tag{5.9}$$

where

$$C_0(\tilde{\delta}) \equiv -\frac{8}{\pi}\int_0^\infty \frac{G'(t)}{t^{\tilde{\delta}-2}}\,dt, \tag{5.10}$$

At this stage it is worthwhile to discuss the method used to obtain the approximating ODEs, as well as the ODEs themselves. First, it is important to remark that in each of the definitions (5.7), (5.8), and (5.10) the variable $\tilde{\delta}$ is a function of $t\tilde{x}$. Moreover, writing $\tilde{w}(\tilde{x}) = \tilde{\beta}(\tilde{x})\tilde{x}^{\tilde{\delta}(\tilde{x})}$ and assuming that $\tilde{\beta}$ and $\tilde{\delta}$ are slowly varying we obtain the approximation

$$\tilde{\delta} \approx \frac{\tilde{x}}{\tilde{w}}\frac{\mathrm{d}\tilde{w}}{\mathrm{d}\tilde{x}},$$

which shows that in fact $\tilde{\delta}$ is a function of $\tilde{x}$, $\tilde{w}$, and $d\tilde{w}/d\tilde{x}$. Thus the terms C_1 and C_2 appearing in (5.6) as well as C_0 appearing in (5.9) represent non-linear terms. This brings into question the benefit of using this approximation. Motivated by the next point, in the following section we will construct solutions by first assuming $\tilde{\delta}$ is constant, solving the ODE, and then obtaining corrections iteratively.

The second point we make involves the suitability of using the approximation (5.2) in the above construction. This was briefly touched on in the $0 < n \leq 1$ where we used that $\tilde{w}(\tilde{s})$ was either in the viscous or the leak-off regimes and was therefore suitably approximated by a function of the form $\tilde{w} = \tilde{\beta}\tilde{x}^{\tilde{\delta}}$, where $\tilde{\beta}$ and $\tilde{\delta}$ did not vary significantly from their counterparts in (4.10) and (4.11) respectively. However, this does not address the question of the suitability of this approximation outside of these spatial regions. For example, we may question in what sense (5.2) is suitable in (5.4) when $\tilde{x}$ is not in the viscous regime. A similar question can be raised for the $n = 0$ case where we simply stated our assumption that $\frac{(\tilde{s}/\tilde{x})^{\tilde{\delta}}}{\tilde{w}}$ does not vary significantly.

To address this question we turn to our discussion of the asymptotic regimes found in §3 and in particular the spatial ordering of the parameter regimes. This discussion revealed that provided $\chi \neq 0$ and $n \neq 0$ there will be three-distinct parameter regions corresponding to toughness, leak-off, and viscosity. Within each such region the solution takes the form of a monomial. The same is true for $\chi = 0$ or $n = 0$ where there are now only two distinct parameter regions. The upshot of this is that within these regions the assumption that $\frac{\tilde{w}(\tilde{s})}{(\tilde{s}/\tilde{x})^{\tilde{\delta}}}$ is approximately constant is appropriate. Moreover, this discussion also reveals that this approximation is not appropriate in the transition regions between parameter regimes where $\tilde{\beta}$ and $\tilde{\delta}$ may undergo sufficiently rapid changes. Therefore, we should expect the errors of the approximating ODE to be concentrated in the transition regions.

5.1 The Constant $\tilde{\delta}$ Approximation

The concluding comments in the section above revealed two key points worth pursuing further. First, in their current form, the approximating ODEs (5.6) and (5.9) provide no clear advantage due to the non-linearities arising from $\tilde{\delta} \approx \tilde{x}\tilde{w}'/\tilde{w}$. Secondly, the

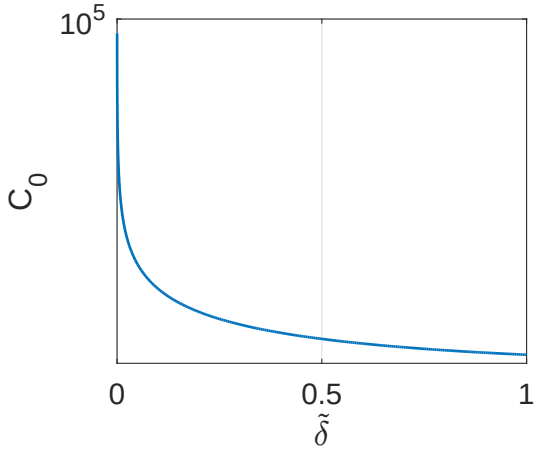

Figure 5.2: Variation in C_0 as $\tilde{\delta}$ varies between $0 \leq \tilde{\delta} \leq 1$.

approximations used to obtain these ODEs are only suitable in those regions where the solution takes the form of a monomial $\tilde{w} = \tilde{\beta}\tilde{x}^{\tilde{\delta}}$ (more specifically in the toughness, leak-off, and viscosity dominating regions). Motivated by these two points, we proceed by fixing the value of $\tilde{\delta}$ within each of the integrals in (5.7), (5.8), and (5.10) to a function only of $\tilde{x}$. Then using the result (see Appendix A.2)

$$\int_0^\infty \frac{G'(t)}{t^\kappa}\,dt = \frac{2\pi\kappa}{(1+\kappa)(1-\kappa)}\tan\left(\frac{\pi}{2}(\kappa+1)\right) \qquad (-2 < \kappa \leq 0), \tag{5.11}$$

we obtain the following closed form expressions for (5.10), (5.7), and (5.8)

$$C_0(\tilde{\delta}) = \frac{16(2-\tilde{\delta})}{(1-\tilde{\delta})(3-\tilde{\delta})}\tan\left(\frac{\pi}{2}(1-\tilde{\delta})\right), \tag{5.12}$$

$$C_1(\tilde{\delta}, n) = \frac{16(2-n-(1+n)\tilde{\delta})}{(1-n-(1+n)\tilde{\delta})(3-n-(1+n)\tilde{\delta})}\tan\left(\frac{\pi}{2}(1-n-(1+n)\tilde{\delta})\right), \tag{5.13}$$

$$C_2(\tilde{\delta}, n) = \frac{16(2-n-(1+2n)\tilde{\delta})}{(1-n-(1+2n)\tilde{\delta})(3-n-(1+2n)\tilde{\delta})}\tan\left(\frac{\pi}{2}(1-n-(1+2n)\tilde{\delta})\right), \tag{5.14}$$

where we emphasize that $\tilde{\delta} = \tilde{\delta}(\tilde{x})$. The use of (5.11) is readily seen to be valid for $0 < n \leq 1$ and $0 < \tilde{\delta} \leq \frac{2-n}{2+n}$ since in this case $-2 < \kappa \leq 0$ is satisfied for each integral appearing in C_0, C_1, and C_2. The same can be said for $n = 0$ when $0 < \tilde{\delta} \leq 1$, but when

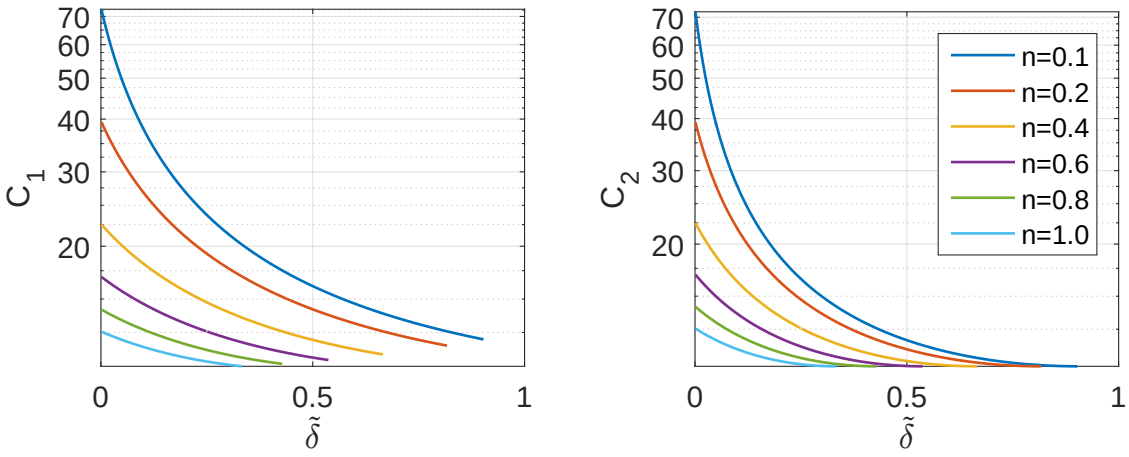

(a) (b)

Figure 5.3: Variation in coefficients C_1 and C_2 as $\tilde{\delta}$ varies between $0 \leq \tilde{\delta} \leq \frac{2-n}{2+n}$ for several $0 < n \leq 1$ values.

$\tilde{\delta} = 0$ we find that the integral appearing in C_0 has $\kappa = -2$ and the identity (5.11) no longer applies. Fortunately, in this case we have $\tilde{x} = 0$ so the coefficient C_0 disappears from the ODE (5.9) altogether.

In Figures 5.2 and 5.3 we see how each of the coefficients C_0, C_1, and C_2 vary with $\tilde{\delta}$. These figures indicate that as n decreases the range of values taken by each coefficient increases, and in particular C_0 diverges as $\tilde{\delta} \to 0$ as expected. When $n \approx 1$ we observe that there is a relatively small change in both coefficients C_1 and C_2 as $\tilde{\delta}$ varies. In the paper by Dontsov and Peirce [6] this relatively small variation motivated setting C_1 and C_2 to two distinct constants that accurately capture individual propagation regimes. We will take the same approach for $0 \leq n \leq 1$, and although, in light of Figures 5.2 and 5.3, this is a rather extreme assumption, comparisons to full numerical results in Chapter 6 will reveal that this is an acceptable approximation.

Having decided to fix the values of the coefficients C_0, C_1 and C_2, or equivalently the values of $\tilde{\delta} \in [0, \frac{2-n}{2+n}]$, the question naturally arises as to what values of $\tilde{\delta}$ should be

chosen. In addressing this question we first focus on the $0 < n \leq 1$ case. We observe that there are two distinguished limits we can deduce from the $0 < n \leq 1$ ODE (5.6). One such limit is when $\tilde{w} \gg \chi$ and therefore the first term dominates (which isolates C_1), whereas for the other limit $\tilde{w} \ll \chi$ and therefore the second term dominates (which isolates C_2). By comparing the resulting behaviour of $\tilde{w}$ implied by (5.6) in these two cases with that implied by the non-linear integral equation (4.8) we can therefore determine what values C_1 and C_2 should take, which in turn will motivate our decision of $\tilde{\delta}$ values.

We focus now on the distinguished limit $\tilde{w} \gg \chi$. Then the ODE (5.6) and its resulting solution become

$$\frac{\mathrm{d}\tilde{w}}{\mathrm{d}\tilde{x}} \sim C_1(\tilde{\delta}, n)\frac{\tilde{x}^{1-n}}{\tilde{w}^{1+n}} \longrightarrow \tilde{w} = \left(1 + \frac{2+n}{2-n}C_1(\tilde{\delta}, n)\tilde{x}^{2-n}\right)^{\frac{1}{2+n}}.$$

On the other hand, as seen in §4.1 the solution to the non-singular integral equation (4.8) has the form $\tilde{w} = \tilde{\beta}\tilde{x}^{\tilde{\alpha}}$ where $\tilde{\beta}$ and $\tilde{\alpha}$ are given by (4.10). Comparing this to the solution obtained from the ODE and noting that the viscous regime dominates for $\tilde{x} \gg 1$ we deduce the requirement that

$$C_1(\tilde{\delta}, n) = \frac{2-n}{2+n}\beta_m^{2+n} = -\frac{2(4-n^2)}{n}\tan\left(\frac{2\pi}{2+n}\right). \tag{5.15}$$

As is easily checked using (5.13) this requirement is met by setting $\tilde{\delta} = \frac{2-n}{2+n}$. Note that in this case the first term in the ODE accurately captures the viscous solution ($\tilde{w} \gg \chi$)) by exhibiting both the correct coefficient $\tilde{\beta}$ and power $\tilde{\alpha}$ in (4.10).

Proceeding as above, we now consider the limit $\tilde{w} \ll \chi$ in which case the ODE (5.6) and it's solution become

$$\frac{\mathrm{d}\tilde{w}}{\mathrm{d}\tilde{x}} \sim C_2(\tilde{\delta}, n)\chi^n\frac{\tilde{x}^{1-n}}{\tilde{w}^{1+2n}} \longrightarrow \tilde{w} = \left(1 + 2\frac{1+n}{2-n}C_2(\tilde{\delta}, n)\chi^n\tilde{x}^{2-n}\right)^{\frac{1}{2(1+n)}}.$$

In this regime the solution of the non-singular integral equation (4.8) takes the form $\tilde{w} = \tilde{\beta}\tilde{x}^{\tilde{\alpha}}$ where the coefficient and power are now given by (4.11). Comparing this

solution to that obtained from the ODE we deduce the requirement that

$$C_2(\tilde{\delta}, n) = \frac{2-n}{2(1+n)}\beta_{cm}^{2(1+n)} = -\frac{32(2-n)(1+n)}{3n(4+n)}\tan\left(\frac{\pi(4+n)}{4(1+n)}\right). \tag{5.16}$$

Using (5.14) we deduce that this requirement is met upon setting $\tilde{\delta} = \frac{2-n}{2(1+n)}$, which corresponds to the correct value of $\tilde{\alpha}$ from (4.11).

To complete this section we now focus on the $n = 0$ ODE (5.9). In this case with $\tilde{\delta}$ fixed the solution is immediately seen to be

$$\tilde{w}(\tilde{x}) = (1 + C_0(\tilde{\delta})\tilde{x}^2)^{\frac{1}{2}}.$$

Motivated by the previous discussion we match this up with the viscous solution which in the limit $n \to 0$ takes on the value $\tilde{w}(\tilde{x}) = 2\sqrt{\pi}\tilde{x}$ and hence we require

$$C_0(\tilde{\delta}) = 4\pi, \tag{5.17}$$

which we see is obtained by taking the limit $\tilde{\delta} \to 1$ in (5.12).

In summary, when $0 < n \leq 1$ we obtain the ODE

$$\frac{\mathrm{d}\tilde{w}}{\mathrm{d}\tilde{x}} = \frac{\gamma_1}{(1+\chi/\tilde{w})^{1-n}}\frac{\tilde{x}^{1-n}}{\tilde{w}^{1+n}} + \frac{\gamma_2\chi}{(1+\chi/\tilde{w})^{1-n}}\frac{\tilde{x}^{1-n}}{\tilde{w}^{2+n}}, \qquad \tilde{w}(0) = 1, \tag{5.18}$$

where

$$\gamma_1 = -\frac{2(4-n^2)}{n}\tan\left(\frac{2\pi}{2+n}\right), \tag{5.19}$$

$$\gamma_2 = -\frac{32(2-n)(1+n)}{3n(4+n)}\tan\left(\frac{\pi(4+n)}{4(1+n)}\right). \tag{5.20}$$

Similarly, for $n = 0$ we have the ODE

$$\frac{\mathrm{d}\tilde{w}}{\mathrm{d}\tilde{x}} = 4\pi\frac{\tilde{x}}{\tilde{w}}, \qquad \tilde{w}(0) = 1. \tag{5.21}$$

5.2 Solutions of the Constant $\tilde{\delta}$ ODE

The simplifications to the original ODEs (5.6) and (5.9) granted by fixing $\tilde{\delta}$ are tremendous. However, even with these simplifications, apart from the special cases of $n = 0$ or $\chi = 0$ the resulting ODE (5.18) does not admit an explicit solution of the form $\tilde{w} = \tilde{w}(\tilde{x})$. We can overcome this difficulty in two different ways. The first is to use a numerical solver such as Matlab's `ode45` to solve the IVP (5.18) numerically for $\tilde{x}$ in some finite range (say $0 \leq \tilde{x} \leq 10^{20}$). For example, upon specifying the grid points `xt` we may determine the solution `wta` through the commands

```
% calcualte ODE coefficients
g1 = -2*(4-n^2)*tan(2*pi/(2+n))/n;
g2 = -32*(2-n)*(1+n)*tan(pi*(4+n)/(4*(1+n)))/(3*n*(4+n));

% solve the constant delta approximating ODE using ode45
odefun = @(x,w) ((1+chi./w).^(n-1)).*(g1./w.^(1+n) + chi*g2./w.^(2+n)).*x.^(1-n);
[~,wta] = ode45(@(X,W)odefun(X,W),xt,1);
```

This approach has the benefits of being sufficiently fast, and moreover it allows the user to determine $\tilde{w}$ values at specified $\tilde{x}$ values.

In the second approach we discard the requirement that the solution be of the form $\tilde{w} = \tilde{w}(\tilde{x})$ and instead use the fact that the ODE is separable to obtain a solution of the form $\tilde{x} = \tilde{x}(\tilde{w})$ given by

$$\tilde{x} = \left[(2-n) \int_1^{\tilde{w}} \frac{(v+\chi)^{1-n} v^{1+2n}}{\gamma_1 v + \gamma_2 \chi} \, dv \right]^{\frac{1}{2-n}}. \tag{5.22}$$

This expression has the benefit that by a suitable change of variables we can map the interval of integration from $[1, \tilde{w}]$ to $[-1, 1]$ thereby making it suitable for standard quadrature rules. The downside to this approach is that to obtain $\tilde{w} = \tilde{w}(\tilde{x})$ we would need to solve an implicit equation. Alternative we could calculate $\tilde{x}$ for a large sample of points $\tilde{w}$ and from this generate an interpolating polynomial solution using, for example, Matlab's `pchip` function. In some cases, such as the $n = 1$ case discussed in [6], the integral ap-

pearing in (5.22) can be evaluated explicitly. However even in this case there is little advantage in evaluating the integral explicitly when a standard quadrature scheme can be done at the same or faster speed and with sufficiently high accuracy.

When $n = 0$ or $\chi = 0$ we are in the more favourable situation wherein we can solve the constant $\tilde{\delta}$ ODE explicitly. In the case of arbitrary $0 \leq n \leq 1$ and $\chi = 0$ we have

$$\tilde{w}(\tilde{x}) = \left(1 + \frac{2+n}{2-n}\gamma_1 \tilde{x}^{2-n}\right)^{\frac{1}{2+n}} \tag{5.23}$$

whereas when $n = 0$ we have

$$\tilde{w}(\tilde{x}) = (1 + 4\pi\tilde{x}^2)^{1/2} \tag{5.24}$$

5.3 The $\tilde{\delta}$-Corrected Solution

In this section we explore the so-called "$\tilde{\delta}$-correction" procedure set out in [6]. This introduces a correction to the constant $\tilde{\delta}$ approximation by iteratively solving for an updated $\tilde{\delta}$ via the approximation $\tilde{\delta} \approx \frac{\tilde{x}}{\tilde{w}}\frac{\mathrm{d}\tilde{w}}{\mathrm{d}\tilde{x}}$. We begin by focusing on the $0 < n \leq 1$ case. As the "zero-order" solution we take the constant $\tilde{\delta}$ solution (5.22) which we repeat here for convenience

$$\tilde{x}_0(\tilde{w}) = \left[(2-n)\int_1^{\tilde{w}} \frac{(v+\chi)^{1-n}v^{1+2n}}{v + b_0\chi}\, dv\right]^{\frac{1}{2-n}} \tag{5.25}$$

where we have defined $b_0 \equiv \gamma_2/\gamma_1$. Substituting this into the constant coefficient ODE (5.6) we obtain the first $\tilde{\delta}$ correction

$$\tilde{\delta}_1 = \frac{\tilde{x}_0(\tilde{w})}{\tilde{w}}\frac{\mathrm{d}\tilde{w}}{\mathrm{d}\tilde{x}}\bigg|_{\tilde{x}=\tilde{x}_0} = \frac{\gamma_1}{(1+\chi/\tilde{w})}\frac{\tilde{x}_0(\tilde{w})^{2-n}}{\tilde{w}^{2+n}}\left(1 + \frac{b_0\chi}{\tilde{w}}\right). \tag{5.26}$$

Since we have $\tilde{\delta}_1 = \tilde{\delta}_1(\tilde{w})$ it follows that (5.6), like the constant $\tilde{\delta}$ ODE (5.18), is separable and hence we can solve for $\tilde{x}$ to obtain the first $\tilde{\delta}$-corrected solution

$$\tilde{x}_1(\tilde{w}) = \left[(2-n)\int_1^{\tilde{w}} \frac{(v+\chi)^{1-n}v^{1+2n}}{C_1(\tilde{\delta}_1(v), n)v + C_1(\tilde{\delta}_2(v), n)\chi}\, dv\right]^{\frac{1}{2-n}}. \tag{5.27}$$

At this stage we remark that in [6], the authors replace the v dependence of $\tilde{\delta}_1$ within the integral, with a dependence on $\tilde{w}$. This renders the C_1 and C_2 terms constant within the integral thereby simplifying the calculation. The reasons for this decision are not clear, but by comparing this to the solution obtained by solving the integral equation (4.8) numerically we find that it gives a better approximation. For this reason, we will be making use of the same approximation, though we emphasize that the reasons for its improved accuracy are not completely understood. Thus, as the first $\tilde{\delta}$-corrected solution we take

$$\tilde{x}_1(\tilde{w}) = \left[\frac{2-n}{C_1(\tilde{\delta}_1(\tilde{w}), n)} \int_1^{\tilde{w}} \frac{(v+\chi)^{1-n} v^{1+2n}}{v + b_1(\tilde{w})\chi}\, dv\right]^{\frac{1}{2-n}}. \tag{5.28}$$

where we have defined $b_1(\tilde{w}) \equiv C_2(\tilde{\delta}_1(\tilde{w}), n)/C_1(\tilde{\delta}_1(\tilde{w}), n)$. By following the same procedure we can find the second $\tilde{\delta}$ correction and so on, though numerical comparisons reveal that beyond the first $\tilde{\delta}$ correction there is a minimal improvement in accuracy. In the $n = 0$ case we obtain analogous results but with the absence of χ terms, and furthermore replacing C_1 with C_0.

In Appendix B.2 and B.3 we have included sample Matlab code for evaluating the zero and first $\tilde{\delta}$-corrected solutions. In this code we have mapped the integration interval to $[-1, 1]$ and have used a 64-point Gauss-Legendre scheme to evaluate the integral.

The next section involves the numerical solution of the full non-singular integral equation (4.8). This is accomplished by first discretizing the integral using Simpson's rule and then solving the resulting non-linear system in the unknowns $W_j \approx \tilde{w}(X_j)$ using (vector) Newton's method. In this context, solutions to the constant $\tilde{\delta}$ will play the role of the initial guess in Newton's method. Since we will be interested in finding $\tilde{w}$ values at specific $\tilde{x}$ values, we will opt to solve the constant $\tilde{\delta}$ ODE numerically using `ode45`. We will then compare solutions obtained in this way to those obtained using the zero- and first-$\tilde{\delta}$ corrected solutions.

Chapter 6

Numerical Solution of Non-linear Integral Equation

In this section we will be solving the non-linear integral equation (4.8) numerically. We begin by discretizing the positive real line using logarithmically distributed points

$$0 < X_1 < \cdots < X_{2N+1} < \infty$$

where we assume $X_1 \ll 1$ so that $\tilde{w}(\tilde{x}) \approx 1$ for all $\tilde{x} \leq X_1$ and $X_{2N+1} \gg 1$ so that $\tilde{w}(\tilde{x}) \approx \beta_m \tilde{x}^{\frac{2-n}{2+n}}$ for all $\tilde{x} \geq X_{2N+1}$. The choice of logarithmatically distributed points is to accommodate the discretization of this large interval. In addition we have chosen to use $2N+1$ points in the discretization to facilitate the use of Simpson's rule in subsequent steps.

Now we evaluate the non-linear integral equation at $\tilde{x} = X_i$ and rewrite it as

$$\tilde{w}(X_i) = 1 + \frac{8}{\pi}\bigg(I_0(X_i, \tilde{w}) + I(X_i, \tilde{w}) + I_\infty(X_i, \tilde{w})\bigg), \tag{6.1}$$

where

$$I_0(X_i,\tilde{w}) = \int_0^{X_1} \frac{G(\tilde{s}/X_i)\tilde{s}^{1-n}}{\tilde{w}(\tilde{s})^{1+n}}\left(1+\frac{\chi}{\tilde{w}(\tilde{s})}\right)^n d\tilde{s}, \tag{6.2}$$

$$I(X_i,\tilde{w}) = \int_{X_1}^{X_{2N+1}} \frac{G(\tilde{s}/X_i)\tilde{s}^{1-n}}{\tilde{w}(\tilde{s})^{1+n}}\left(1+\frac{\chi}{\tilde{w}(\tilde{s})}\right)^n d\tilde{s}, \tag{6.3}$$

$$I_\infty(X_i,\tilde{w}) = \int_{X_{2N+1}}^{\infty} \frac{G(\tilde{s}/X_i)\tilde{s}^{1-n}}{\tilde{w}(\tilde{s})^{1+n}}\left(1+\frac{\chi}{\tilde{w}(\tilde{s})}\right)^n d\tilde{s}. \tag{6.4}$$

In what follows we will discretize $I(X_i,\tilde{w})$, and find leading order approximations for I_0 and I_∞ as functions of X_1, X_i, and X_{2N+1} respectively.

We introduce the vector $\mathbf{W} = (W_1,...,W_{2N+1})^T$ where each W_i approximates $\tilde{w}(X_i)$ by solving the resulting non-linear system. In addition we define $G_{ij} \equiv G(X_j/X_i)$ so that for each $i = 1,...,2N+1$ the Simpson's rule discretization of $I(\tilde{w},X_i)$ becomes

$$\begin{aligned} I(X_i,\mathbf{W}) \approx \frac{1}{6(2-n)}\sum_{j=1}^{N}(X_{2j+1}^{2-n}-X_{2j-1}^{2-n})\Bigg[&\frac{G_{i,2j-1}}{W_{2j-1}^{n+1}}\left(1+\frac{\chi}{W_{2j-1}}\right)^n \\ &+4\frac{G_{i,2j}}{W_{2j}^{n+1}}\left(1+\frac{\chi}{W_{2j}}\right)^n+\frac{G_{i,2j+1}}{W_{2j+1}^{n+1}}\left(1+\frac{\chi}{W_{2j+1}}\right)^n\Bigg], \end{aligned} \tag{6.5}$$

where we remark we have made the substitution $\tilde{s}^{1-n}d\tilde{s} = \frac{1}{2-n}d(\tilde{s}^{2-n})$ prior to using Simpson's rule. In particular this substitution allows us to make the terms in square brackets depend solely on $\mathbf{W}$.

Before approximating $I_0(X_i,\mathbf{W})$ and $I_\infty(X_i,\mathbf{W})$ we make note of the following series

$$G(t) = 4-4t^2\sum_{k=0}^{\infty}\frac{t^{2k}}{(2k+1)(2k+3)}, \qquad (0\le t\le 1), \tag{6.6}$$

$$G(t) = \frac{4}{t^2}\sum_{k=0}^{\infty}\frac{t^{-2k}}{(2k+1)(2k+3)}, \qquad (1\le t). \tag{6.7}$$

The convergence of the series in the designated intervals is easily obtained by using the ratio test and by comparing it to the series $\sum_{k=1}^{\infty}k^{-2}$. To approximate $I_0(X_i,\mathbf{W})$ we use

(6.6) and $\tilde{w}(\tilde{s}) \approx 1$ for all $\tilde{s} \leq X_1$ to obtain

$$I_0(X_i) \approx \frac{(1+\chi)^n}{2-n} X_1^{2-n} \left[4 - 4 \sum_{k=0}^{\infty} \frac{2-n}{(2k+4-n)(2k+1)(2k+3)} \left(\frac{X_1}{X_i} \right)^{2k+2} \right]. \qquad (6.8)$$

By combining $(2-n)/(2k+4-n) \leq 1$ with (6.6) and $0 \leq G(t) \leq 4$ (see Figure 5.1) we obtain the bounds

$$0 \leq 4 \sum_{k=0}^{\infty} \left(\frac{2-n}{2k+4-n} \right) \frac{1}{(2k+1)(2k+3)} \left(\frac{X_1}{X_i} \right)^{2k+2} \leq 4 - G(X_1/X_i) \leq 4,$$

whence we deduce that the term in square brackets in (6.8) is at most $O(1)$. Hence $I_0 = O(X_1^{2-n})$ and since $X_1 \ll 1$ it follows that I_0 is negligibly small and will therefore be ignored.

The approximation of $I_\infty(X_i, \mathbf{W})$ is more involved than that of $I_0(X_i, \mathbf{W})$ and furthermore results in a non-negligible contribution whenever $i = 2N+1$. This time we use $\tilde{w}(\tilde{s}) \approx \beta_m \tilde{s}^{\frac{2-n}{2+n}}$ for all $\tilde{s} \geq X_{2N+1}$ and (6.7) to obtain

$$I_\infty(X_i) \approx \sum_{p=0}^{\infty} \frac{4c_p}{\beta_m^{n+1}} X_{2N+1}^{1-\frac{2n}{2+n}-p\frac{2-n}{2+n}} \sum_{k=0}^{\infty} \frac{(X_{2N+1}/X_i)^{-2k-2}}{(2k+1+\frac{2n}{2+n}+p\frac{2-n}{2+n})(2k+1)(2k+3)}, \qquad (6.9)$$

where each c_p is the coefficient of $\tilde{s}^{p(2-n)/(2+n)}$ in the series expansion of $(1+\frac{\chi}{\beta_m \tilde{s}^{(2-n)/(2+n)}})^n$. Now using (6.7) we have

$$0 \leq 4 \sum_{k=0}^{\infty} \frac{(X_{2N+1}/X_i)^{-2k-2}}{(2k+1+\frac{2n}{2+n}+p\frac{2-n}{2+n})(2k+1)(2k+3)} \leq G(X_{2N+1}/X_i) \leq 4,$$

whence the coefficient of each $X_{2N+1}^{1-\frac{2n}{2+n}-p\frac{2-n}{2+n}}$ in (6.9) is at most $O(1)$ and therefore

$$I_\infty(X_i) = \frac{4}{\beta_m^{n+1}} X_{2N+1}^{\frac{2-n}{2+n}} \sum_{k=0}^{\infty} \frac{(X_{2N+1}/X_i)^{-2k-2}}{(2k+1+\frac{2n}{2+n})(2k+1)(2k+3)} + O\left(X_{2N+1}^{-\frac{2n}{2+n}} \right). \qquad (6.10)$$

It remains to approximate the infinite series making up the coefficient of $X_{2N+1}^{\frac{2-n}{2+n}}$. When $i < 2N+1$ the terms in this infinite series decay exponentially like $(X_i/X_{2N+1})^{2k+2}$ and we can therefore truncate the sum after one term obtaining

$$\sum_{k=0}^{\infty} \frac{(X_{2N+1}/X_i)^{-2k-2}}{(2k+1+\frac{2n}{2+n})(2k+1)(2k+3)} = \frac{2+n}{3(2+3n)} \left(\frac{X_i}{X_{2N+1}} \right)^2 + O\left(\left(\frac{X_i}{X_{2N+1}} \right)^4 \right), \quad (6.11)$$

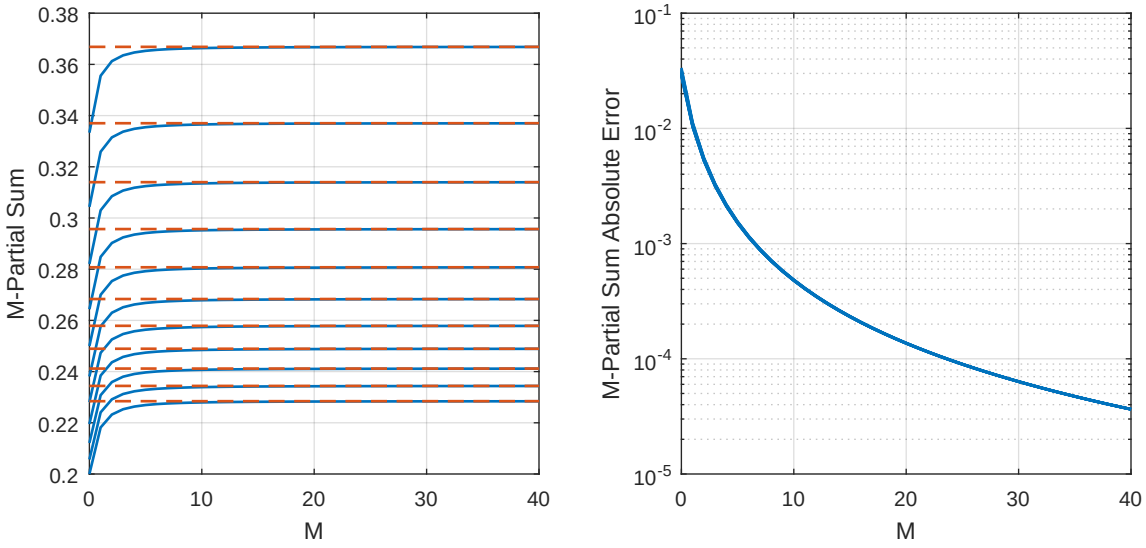

Figure 6.1: Convergence of partial sums making up coefficient of $X_{2N+1}^{\frac{2-n}{2+n}}$ in (6.10). The left pane shows values of the partial sums (solid lines) and infinite sums approximated with $M = 10^4$ (dashed lines) for values of $n = 0$ at the top and $n = 1$ at the bottom in 0.10 steps. The right pane shows the absolute error of partial sums (note that this plot is actually showing a small band that includes all the n values plotted in the left pane).

which has a small error due to the logarithmic distribution of the sample points. When $i = 2N+1$ the terms in the series decay algebraically like k^{-3} which implies that truncating the sum after the first M terms will yield an error that is $O(M^{-2})$. This means that to get an acceptable error in the coefficient, say of the order of 10^{-2}, we will need to take at least 10 terms before truncating the sum (see Figure 6.1). Since $I_\infty(X_i)$ is independent of $\mathbf{W}$ we can compute it prior to solving the resulting non-linear system, thereby saving computation time.

With $I(X_i, \mathbf{W})$ given by (6.5), $I_0(X_i) \approx 0$, and $I_\infty(X_i)$ given by appropriately truncating the sum in (6.10) we therefore obtain the non-linear system of equations

$$A_i \equiv 1 + \frac{8}{\pi}\Big(I(X_i, \mathbf{W}) + I_\infty(X_i)\Big) - W_i = 0, \qquad i = 1, ..., 2N + 1, \tag{6.12}$$

which we can solve using the vector Newton's method. The initial guess for Newton's

method is taken to be the solution of the constant $\tilde{\delta}$ ODE discussed in §5.1. Due to the large values we expect the later entries of $\mathbf{W}$ to take, we will be using a relative change in the solution between iterations for the stopping criterion. The details of the numerical computation of $\tilde{w}$ using this method can be found in the code in Appendix B.1. In this code we see that we have chosen $M = 20$ when calculating the coefficient from (6.10), which according to Figure 6.1 has an associated error of approximately 10^{-4}.

In the following section we will explore the performance of this numerical solver through a variety of numerical experiments. This will be followed by a brief overview of the qualitative characteristics of the solutions obtained by this method. In the final section we will use the solutions of the full non-singular integral equation to compare the accuracy of the solutions obtained by solving the approximating ODE using each of the three methods found in §5: the solution found using `ode45`, and the zero and first $\tilde{\delta}$ corrected solutions.

6.1 Performance of Non-Singular Integral Equation Solver

We will gauge the performance of the numerical solver discussed above by exploring how three quantities – the total computation time, maximum number of iterations, and maximum residual – vary with the numerical parameter N, and the problem parameters n and χ. This was done by solving the non-linear system with Newton's method where we have chosen $X_1, ..., X_{2N+1}$ to consist of $2N+1$ logarithmically distributed points between 10^{-10} and 10^{15}. In each simulation we have fixed the tolerance (i.e. the maximum relative difference between iterations at which Newton's method stops) to 10^{-3}, and the maximum number of iterations to 500. Moreover, for each value of $n = 0, 0.1, 0.2, ..., 1$ we have calculated the maximum of each of the three performance parameters over the range of $10^{-5} \leq \chi \leq 10^{5}$.

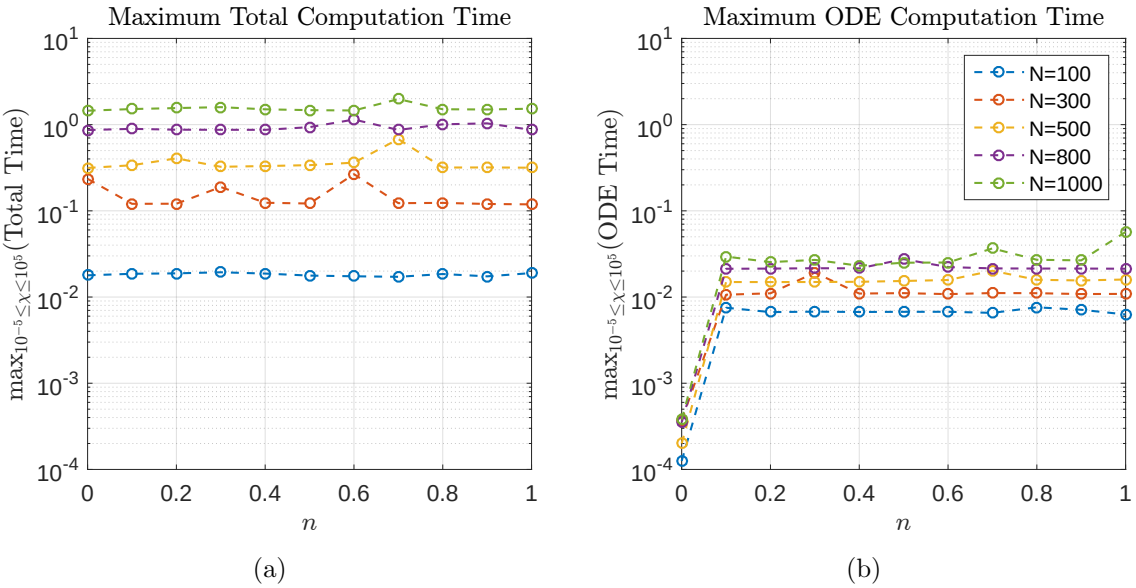

(a) (b)

Figure 6.2: Maximum total computation time (a) and ODE computation time (b) measured in seconds, where the maximum is taken over $10^{-5} \leq \chi \leq 10^5$.

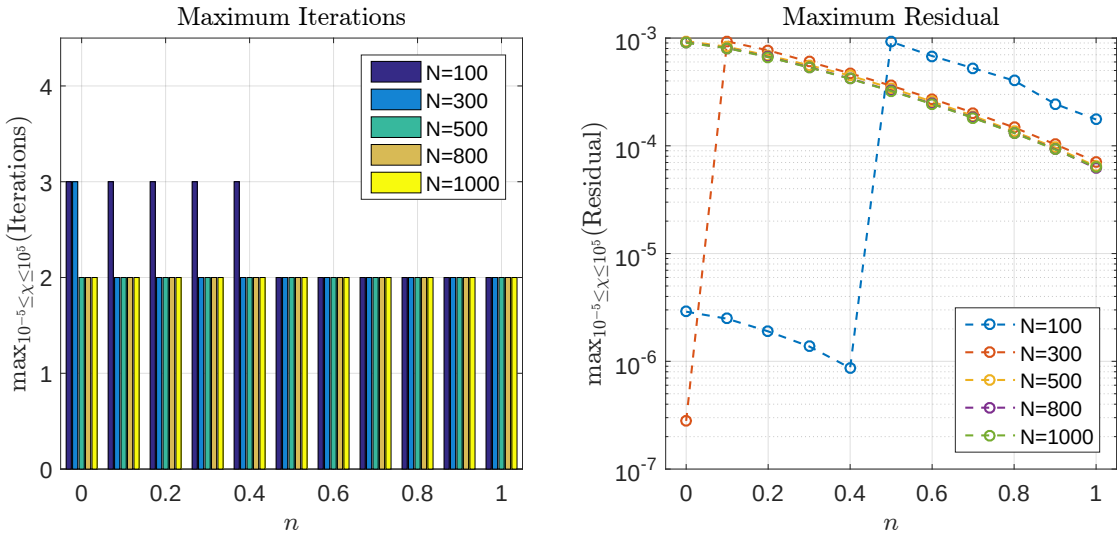

(a) (b)

Figure 6.3: Maximum number of iterations (a) and final residual (b) for Newton's method, where the maximum is taken over $10^{-5} \leq \chi \leq 10^5$.

In Figure 6.2 we have plotted the maximum computation time on the left-hand side, while on the right side we have included the component of that time dedicated to solving the constant $\tilde{\delta}$ ODE using `ode45`. This figure reveals that the total computation time appears to remain constant as n is varied but, as expected, increases with increasing values of N. The same trend is present for the ODE computation time, except when $n = 0$ for which we have an exact solution to the constant $\tilde{\delta}$ ODE given by (5.24).

Next, Figure 6.3 shows how the maximum number of iterations and maximum residual vary with n. The left pane of the figure reveals that the program typically halts after two iterations regardless of the values of N and n being used. Moreover, as indicated by the right pane of the figure, the desired tolerance is typically surpassed. These two observations suggest that the initial guess, i.e. that obtained by solving the approximating ODE with `ode45`, is already very close to the actual solution. We will be exploring this suggestion further in the final section where we compare solutions to the approximating ODE with that obtained by solving the full non-singular integral equation.

6.2 Qualitative Properties of the Numerical Solution

This brief sections showcases some of the quantitative properties of solutions to the non-singular integral equation (4.8). In the left panes of Figures 6.4 to 6.6 we have collected a color map showing how the fracture opening $\tilde{w}$ varies with both $\tilde{x}$ and χ. The right pane of each figure shows some sample solutions o $\tilde{w}$ versus $\tilde{x}$ for values of $\chi = 10^{-5}, 10^{3}, 10^{5}$. We have omitted the $n = 0$ case since then there is no dependence on χ which would otherwise trivialize the figure. In each simulation we have used the following numerical parameters (see Appendix B.1 for definitions)

```
% numeric solution parameters
p0 = -10; p1 = 15; N = 500; ittmax = 500; tol = 1e-3;
```

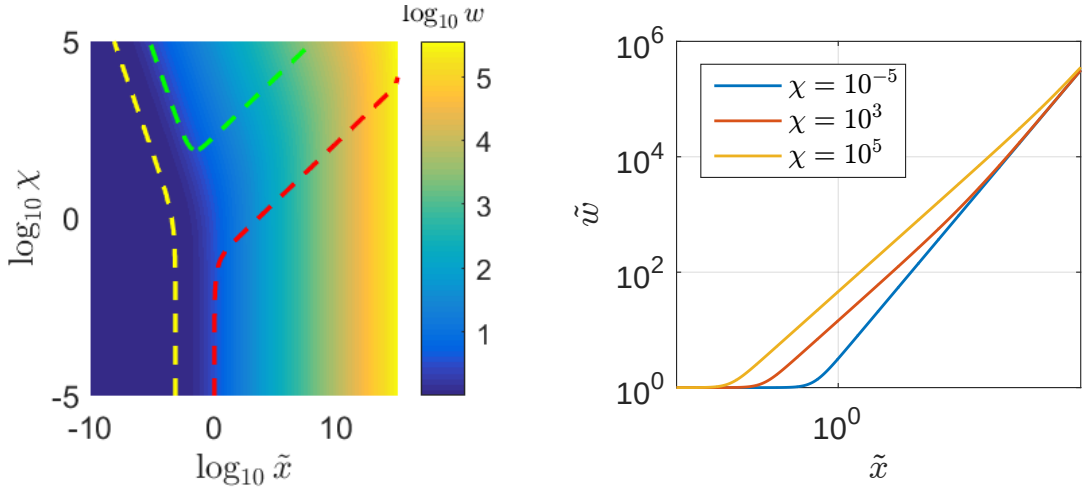

Figure 6.4: Numerical results for n = 1.

In the left pane of each of Figures 6.4 to 6.6 we have also include dashed yellow (left), green (center), and red (right) lines which indicate the boundaries of the toughness, leak-off, and viscosity regimes respectively. Within the region left of the dashed yellow line the relative difference between the numerical solution $\tilde{w}$ and the toughness solution $\tilde{w}_k = 1$ is less than 10^{-2} (i.e. $|\tilde{w} - \tilde{w}_k|/\tilde{w}_k < 10^{-2}$). Inside the region bounded by the dashed green line the relative difference between the numerical solution and the $\tilde{w}$ and the leak-off solution $\tilde{w}_c = \beta_{cm}\chi^{\frac{n}{2(1+n)}}\tilde{x}^{\frac{2-n}{2(1+n)}}$ is less than 10^{-2} (i.e. $|\tilde{w} - \tilde{w}_c|/\tilde{w}_c < 10^{-2}$). On the other hand in the region right of the dashed red line the relative difference between the numerical solution $\tilde{w}$ and the viscous solution $\tilde{w}_m = \beta_m \tilde{x}^{(2-n)/(2+n)}$ is less than 10^{-2} (i.e. $|\tilde{w} - \tilde{w}_m|/\tilde{w}_m < 10^{-2}$). The right pane of each figure plots sample solutions (i.e. $\tilde{w}$ versus $\tilde{x}$) for three distinct χ values. From these figures we can already draw some conclusions as to the behaviour of the fracture opening as χ and n are varied. For fixed n we see that as χ increases the (leak-off) region situated between the toughness and viscosity boundaries grows. However the growth of this intermediate region is stunted as n decreases which can be seen by comparing the left panes of each figure. This is also supported by the

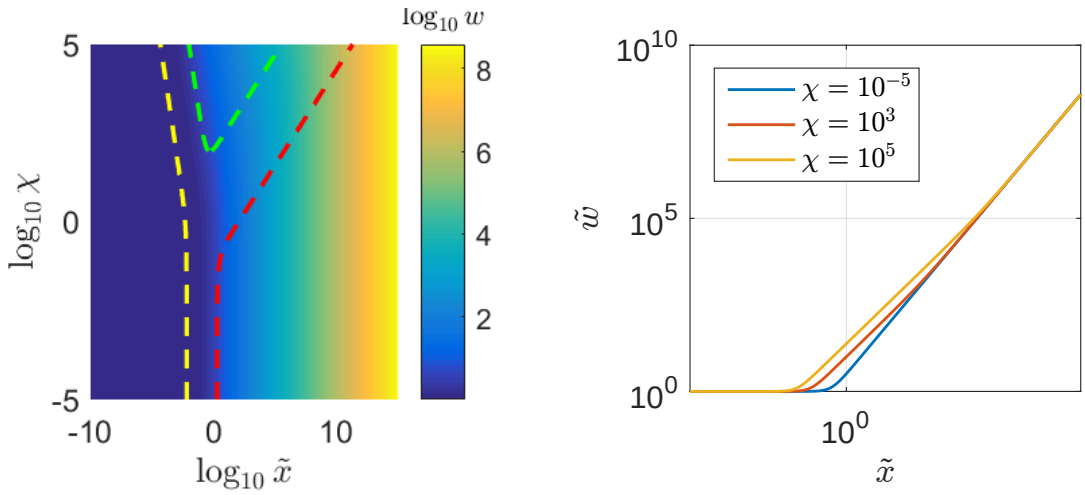

Figure 6.5: Numerical results for n = 0.60.

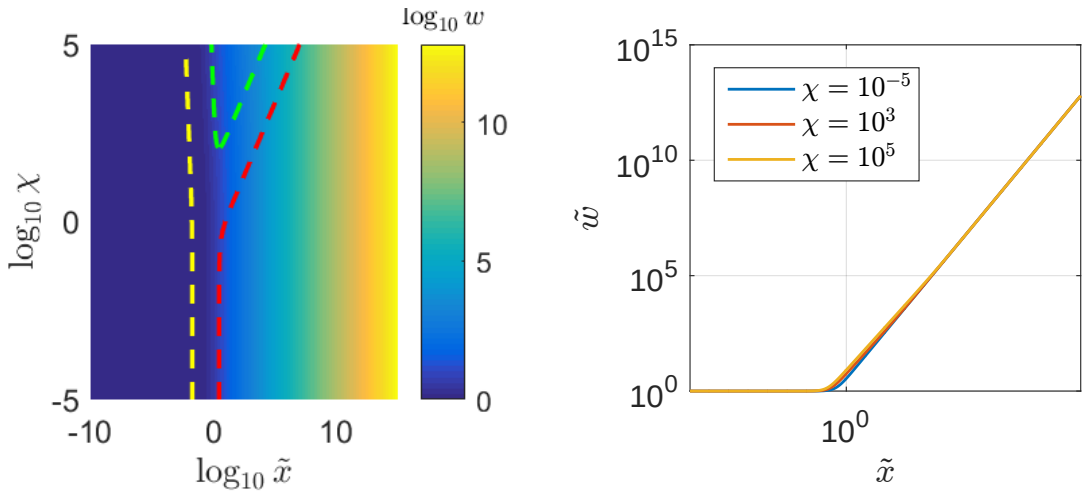

Figure 6.6: Numerical results for n = 0.20.

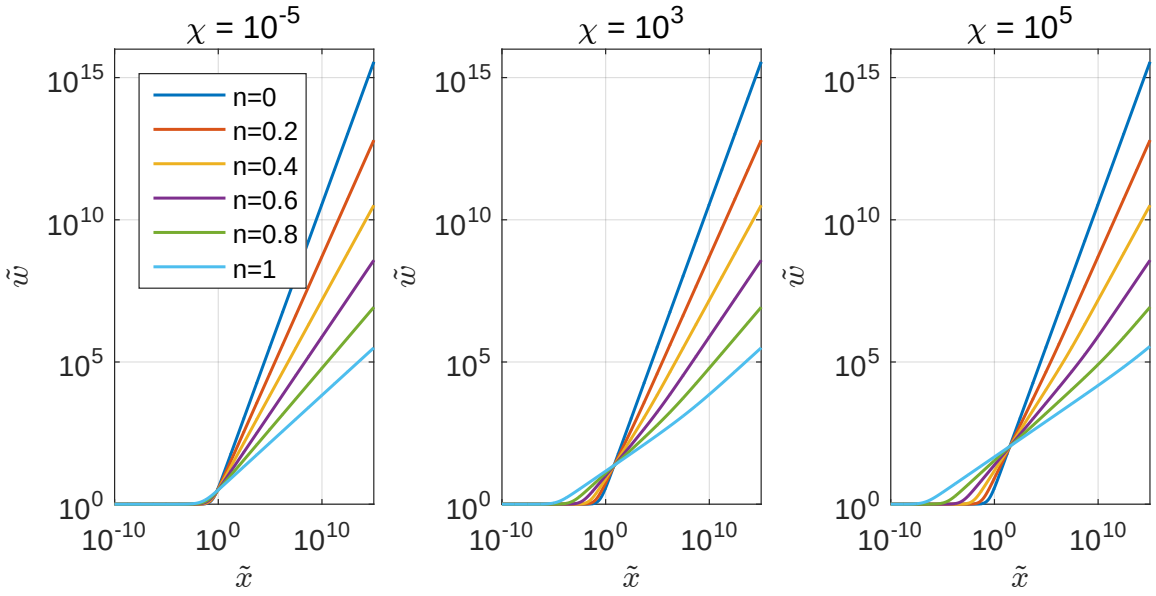

Figure 6.7: Plots of solutions $\tilde{w}(\tilde{x})$ for various n values (see legend) and $\chi = 10^{-5}, 10^{3}, 10^{5}$.

right pane of each figure which shows a decreasing dependence on χ for lower values of n. This effect culminates when $n = 0$, which, as already mentioned, we have omitted in the present plots since this case exhibits no χ dependence (as is clear from the governing equation (4.8)).

Using the same numerical parameters as above, we now explore how the behaviour of the fracture opening changes as n is varied. For this comparison it is important to recall the scaling (4.7) in which the length scale l depends on the parameter n. Figure 6.7 shows the solution $\tilde{w}$ for various values of n and for $\chi = 10^{-5}, 10^{3}, 10^{5}$. As expected we see that the $n = 0$ solution is independent of χ and the dependence on χ becomes more pronounced as n increases. From these plots we also see that for $\tilde{x}$ approximately smaller than 1 the fracture opening is larger with greater values of n, but that the opposite is true for values of $\tilde{x}$ approximately greater than 1. This behaviour is best understood by recalling the asymptotic propagation regimes introduced in §3 and in particular the

change of the power α with n depicted in Figure 3.1. There we immediately see that, apart from α_k, higher powers of n result in smaller values of α and therefore a smaller slope on the plot of $\log \tilde{w}$ versus $\log \tilde{x}$.

6.3 Comparison to Approximating ODE

We conclude this chapter by comparing the accuracy between the solution obtained using `ode45`, the zero $\tilde{\delta}$-corrected solution, and the first $\tilde{\delta}$-corrected solution. In each case we will be making comparisons to the solution obtained by solving the full non-singular integral equation (4.8) numerically as discussed in the first section of this chapter. To reduce errors due to the discretization of the integral equation, we will be using a large mesh point count of $N = 5,000$. Notice that since we are using Simpson's rule, and referring to the code found in Appendix B.1, this corresponds to $2N + 1 = 10,001$ mesh points. In addition, to reduce the errors from truncating the infinite integral appearing in (4.8) we will be taking mesh points in the range 10^{-10} to 10^{20}, but only drawing comparisons in the truncated region of 10^{-10} to 10^{15}. The other parameters in the numerical solver that we are using include a maximum number of iterations of `ittmax = 500` and halting tolerance of `tol = 1e-10`.

For our first comparison we consider the case of $n = 0$. In Figure 6.8 we show how the relative error between the full numerical solution and each of the three approximations varies with $\tilde{x}$. In this figure we remark that the `ode45` and the zero $\tilde{\delta}$-corrected solution are nearly identical, as is expected since they are both solutions to the same ODE. Moreover, the maximum relative error is 0.062 for the `ode45` and zero $\tilde{\delta}$-corrected solutions, whereas it is 0.048 for the first $\tilde{\delta}$-corrected solution. Next, in Figure 6.9 we have included the relative difference between these solutions with the regime solutions $\tilde{w}_k = 1$ and $\tilde{w}_m = \sqrt{4\pi}\tilde{x}$. These figures reveal that in the appropriate spatial regimes each of the approximating

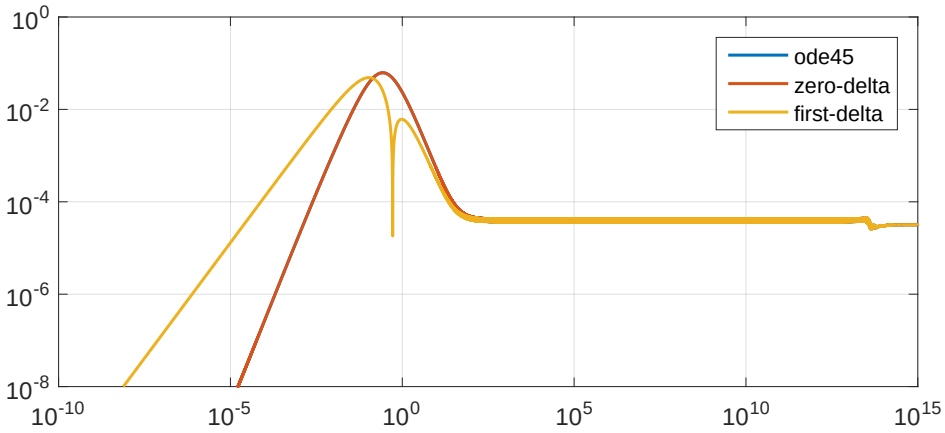

Figure 6.8: Relative error between full numerical solution and solutions to the approximating ODE for $n = 0$. For `ode45` and zero $\tilde{\delta}$-corrected solution the maximum relative error is ≈ 0.062, while for the first $\tilde{\delta}$-corrected solution it is 0.048.

ODE solutions fully capture the asymptotic solutions $\tilde{w}_k$ and $\tilde{w}_m$.

Next for each value of $n = 0.2, 0.4, 0.6, 0.8, 1$ we consider the relative error for $\chi = 10^{-5}, 10^{0}, 10^{5}$. These results are shown in Figures 6.10 – 6.14 for $n = 0.2, ..., 1.0$ respectively. In each such figure we observe that the first $\tilde{\delta}$-corrected solution provides a significant advantage over the `ode45` and zero $\tilde{\delta}$-corrected solutions. Perhaps one of the most significant conclusions we can draw from these figures is that for $n \geq 0.4$ the maximum relative error of the first $\tilde{\delta}$-corrected solution is at most 10^{-2}. Computationally, this observation is very important because it means we can effectively use the significantly less computationally intensive first $\tilde{\delta}$-corrected solution rather than the full numerical solution of the non-singular integral equation. For values of $n < 0.4$ we are no longer in this desirable position and it is likely better not to fully rely on the first $\tilde{\delta}$-corrected solution unless some other means of improving its accuracy are found.

Our final commentary on the approximating ODE solutions revolves around the "bump" features present in Figure 6.8 and Figures 6.10 – 6.14. Motivated by the derivation of the approximating ODE, we claim that these bumps correspond to transition regions

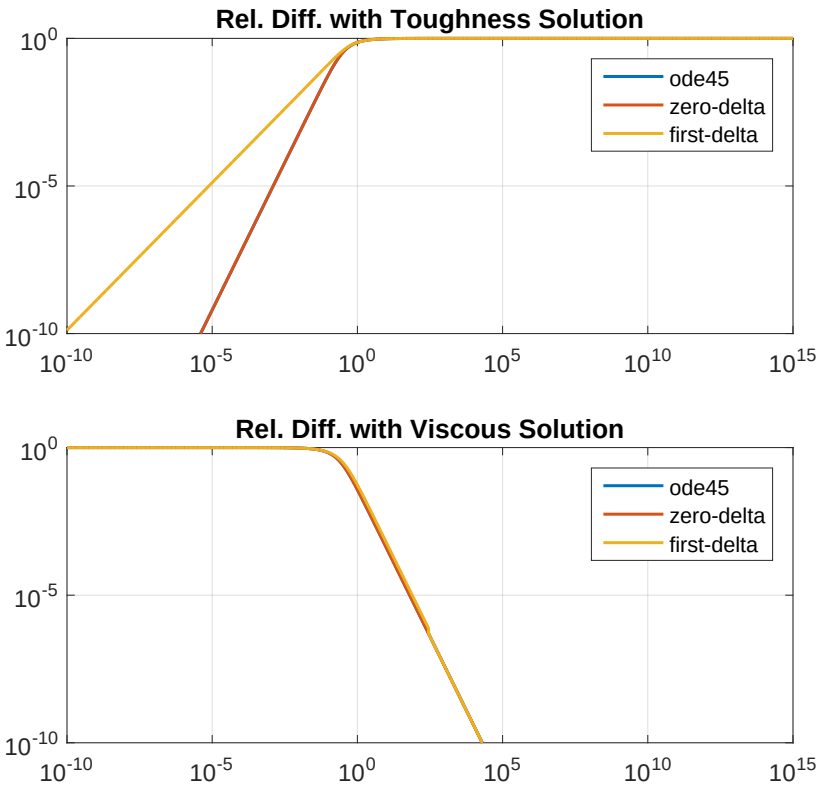

Figure 6.9: Relative difference of approximating ODE solutions with regime solutions (toughness and viscosity).

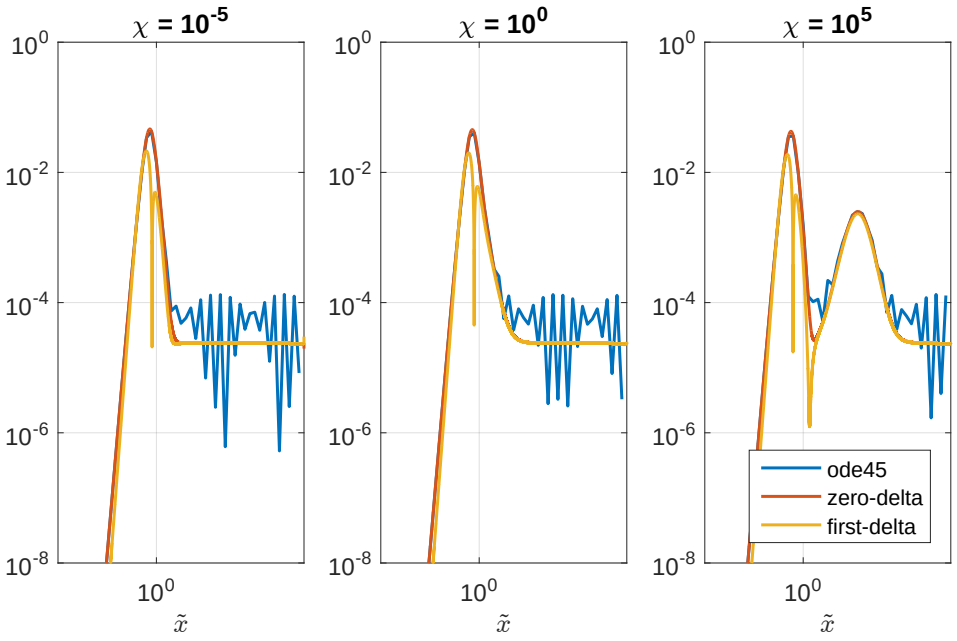

Figure 6.10: Relative error between full numerical solution and solutions to the approximating ODE for $n = 0.2$.

between each of the propagation regimes (toughness, leak-off, and viscosity) as this is where $\tilde{\delta}$ undergoes a transition. Indeed, for $n = 0$ by comparing Figures 6.8 and 6.9 we see that the bump in the former occurs in the region where the latter indicates a deviation from the toughness solution but the beginning of convergence towards the viscous solution. To support this claim for $n > 0$ we have included Figures 6.15 – 6.17 which show the relative error for values of $\chi = 10^5, 10^0, 10^{-5}$ respectively. Each figure includes three panes corresponding to values of $n = 0.2, 0.5, 0.8$. We remark that we have ignored the solution obtained using `ode45` so as not to clutter the plots. In addition, each figure includes two or three dashed vertical lines which indicate the boundaries of the toughness (black), leak-off (green), and viscous (red) regimes defined using the same criteria as was used in Figures 6.4 – 6.6. In particular, the region to the left of the black dashed line corresponds to the toughness regime, the region in between the yellow dashed lines to the leak-off

regime, and the region to the right of the red dashed line to the viscous regime. These figures support our claim that peaks occur at the transitions between different propagation regimes. Moreover, the relative severity of bumps can be explained by referring to Figure 3.1, since in general the transition from the toughness to the leak-off region corresponds to a larger jump in the power α than does the transition from the leak-off to the viscosity regime (i.e. $\alpha_{cm} - \alpha k > \alpha_m - \alpha_{cm}$).

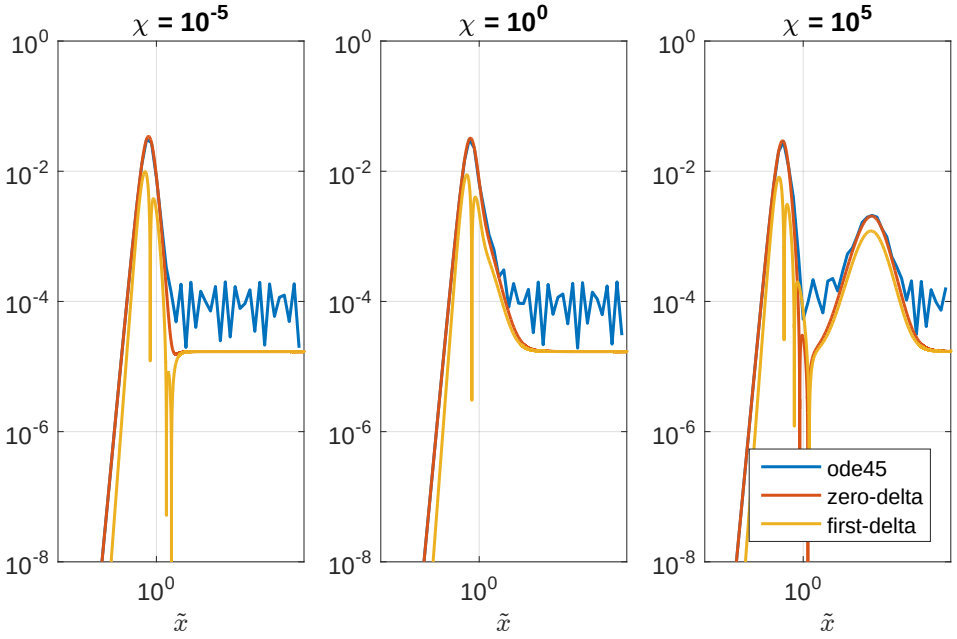

Figure 6.11: Relative error between full numerical solution and solutions to the approximating ODE for $n = 0.4$.

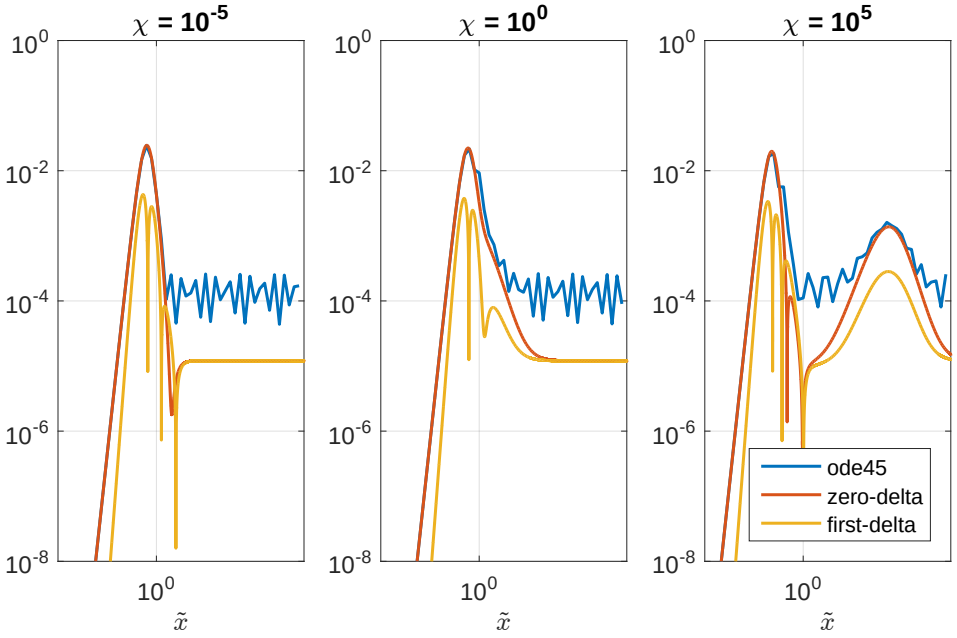

Figure 6.12: Relative error between full numerical solution and solutions to the approximating ODE for $n = 0.6$.

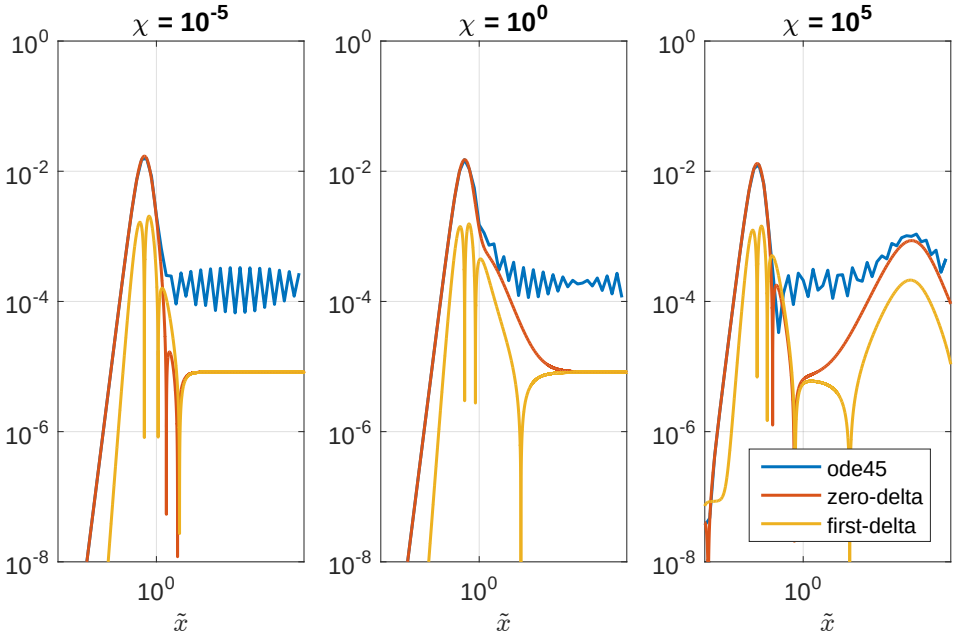

Figure 6.13: Relative error between full numerical solution and solutions to the approximating ODE for $n = 0.8$.

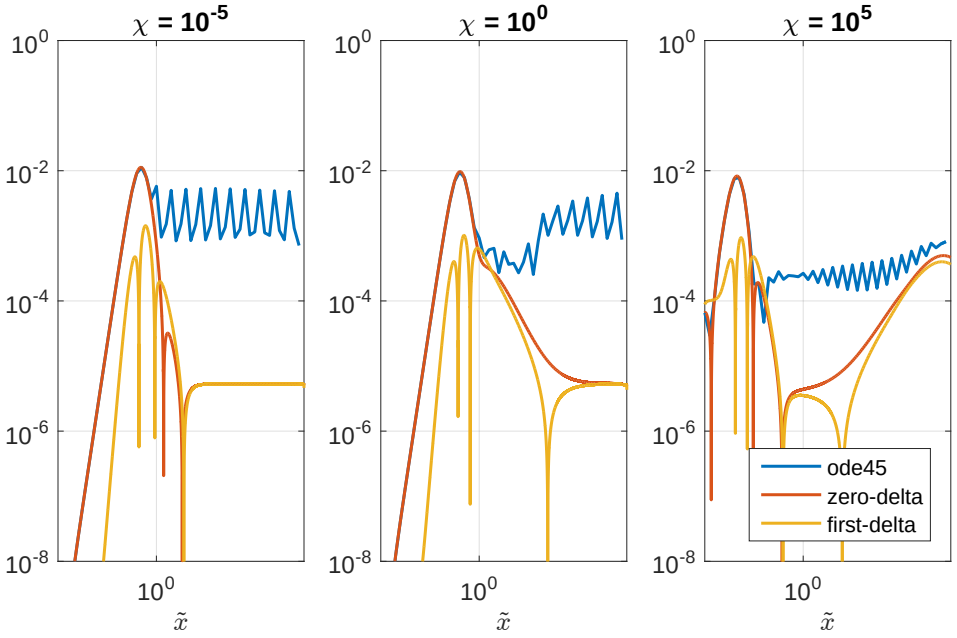

Figure 6.14: Relative error between full numerical solution and solutions to the approximating ODE for $n = 1$.

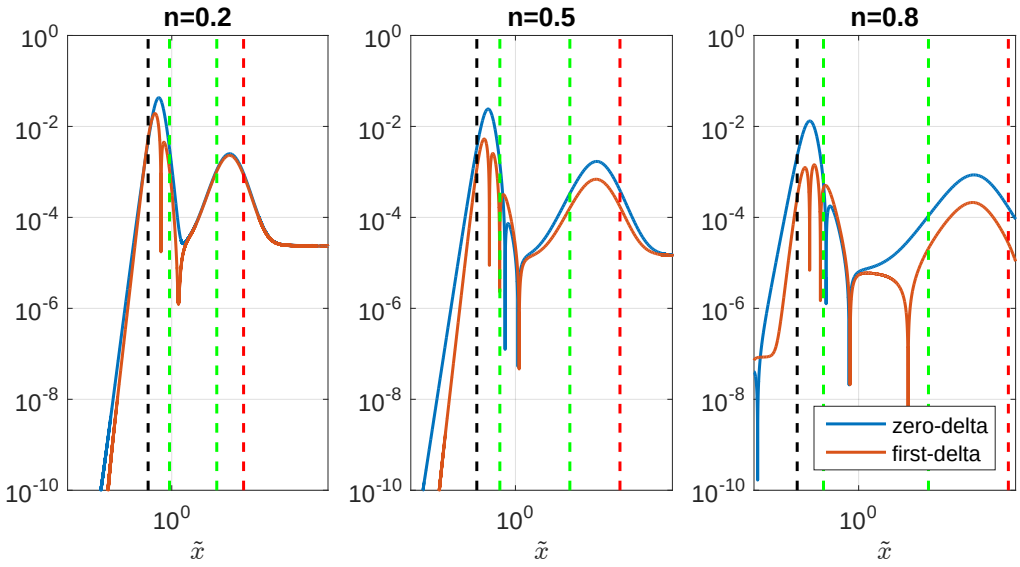

Figure 6.15: Relative error of zero- and first-delta corrected solution for $\chi = 10^5$ with dashed vertical lines showing regime boundaries.

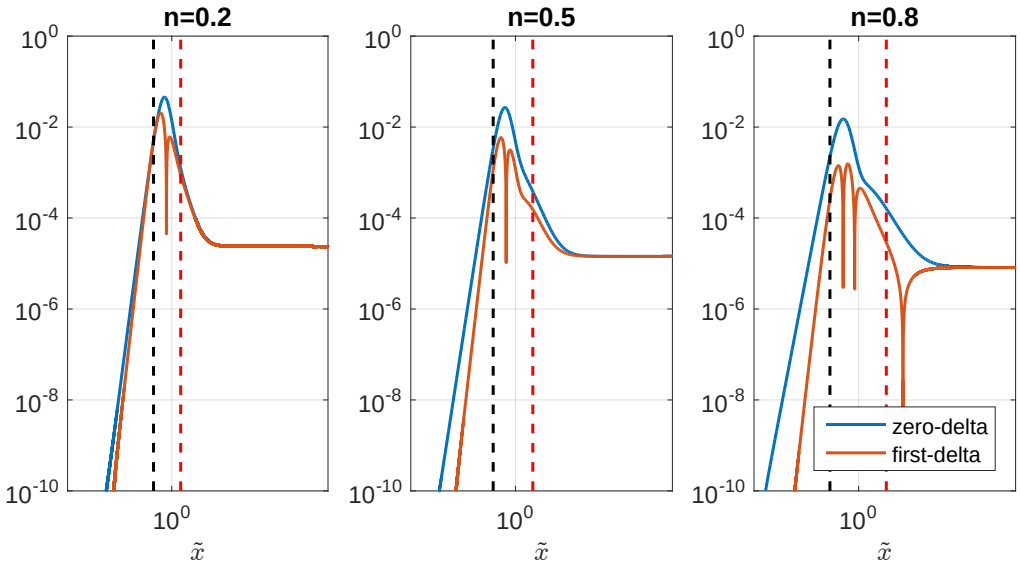

Figure 6.16: Relative error of zero- and first-delta corrected solution for $\chi = 10^0$ with dashed vertical lines showing regime boundaries.

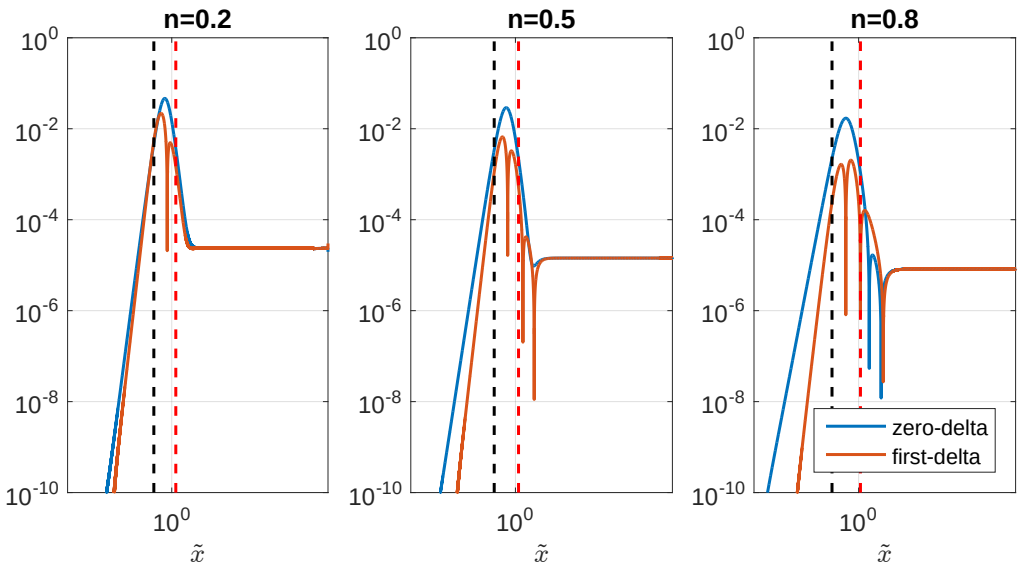

Figure 6.17: Relative error of zero- and first-delta corrected solution for $\chi = 10^{-5}$ with dashed vertical lines showing regime boundaries.

Chapter 7

Conclusion

In this thesis we have considered the problem of a semi-infinite hydraulic fracture under plane strain conditions driven by a shear-thinning power-law fluid. The motivation for studying the semi-infinite fracture arises from its close connection to the tip behaviour of a finite fracture [19] and its relevance to their numerical simulation. Furthermore, we have focused on shear-thinning power-law fluids as this is expected to be the dominant fracturing fluid rheology in oil reservoir stimulation operations [8, 3]. Our model uses Poiseuille's law for a power-law fluid to describe the fracturing fluid's motion, but otherwise neglects the power-law rheology when describing fluid leak-off. This is based on the underlying assumption that the power-law properties of the fracturing fluid arise from the addition of filter-cake-building polymers, which themselves do not experience leak-off.

The main contribution of this thesis has been to expand on the work of Dontsov and Peirce [6] to accommodate shear-thinning power-law fluids. In particular, in Chapter 3 we have included a detailed derivation of the asymptotic solutions that dominate in each of the three propagation regimes. This was followed in Chapters 4 and 5 by reformulating the governing equations to a non-singular integral equation and then reducing it to an approximating ODE. In solving the approximating ODE we considered three methods,

the last of which involved the use of the "delta-correction" method outlined in [6]. This method involves evaluating two integrals, which is easily accomplished using standard quadrature rules, and therefore potentially represents a computationally fast alternative for determining the fracture's tip behaviour.

In Chapter 6 we considered a numerical scheme for solving the non-singular integral equation in which the integral was first discretized using Simpson's rule and the resulting non-linear algebraic system was solved using Newton's method. As a first guess in the Newton's method we used the solution obtained by solving the approximating ODE using Matlab's `ode45` function. The latter part of Chapter 6 focused on comparing the solutions to the approximating ODE to those obtained by solving the non-singular integral equation. These comparisons revealed that the solutions to the approximating ODE are in good agreement with the full numerical solution. In particular, for values of $0 \leq n < 0.4$ the maximum relative error was found to be about 6% whereas for $0.4 \leq n \leq 1$ the first delta-corrected solution yielded a maximum relative error that is less than 1%. Thus, at least for $n \geq 0.4$ the first delta-corrected solution could effectively replace the more computationally intensive solution obtained by solving the non-singular integral equation.

We will conclude by listing some directions for future study. This list will be limited to those directions most relevant to the work presented above. For a more general overview and future problems we direct the reader to the recent review article by Detournay [4]. In no particular order, the proposed directions for future study include:

1. A rigorous derivation and error analysis of the approximating ODE, as well as of the first delta-corrected solution.

2. Finding an improved method of approximating solutions to the non-singular integral equation for values of $n < 0.4$, capable of obtaining relative errors that are $\leq 1\%$.

3. Exploring the effect of the power-law rheology on fluid lag, and in particular determining if, as is the case for Newtonian fluids, the lag region is negligible under common field conditions.

4. Implementing the tip solutions obtained using methods from this thesis in the case of a penny-shaped fracture driven by a power-law fluid.

Bibliography

[1] J. Adachi, E. Siebrits, A. Peirce, and J. Desroches. Computer simulation of hydraulic fractures. *International Journal of Rock Mechanics and Mining Sciences*, 44(5):739–757, 2007.

[2] J. I. Adachi. Fluid-driven fracture in permeable rock, 2001. Copyright - Database copyright ProQuest LLC; ProQuest does not claim copyright in the individual underlying works; Last updated - 2016-05-05.

[3] J. I. Adachi and E. Detournay. Self-similar solution of a plane-strain fracture driven by a power-law fluid. *International Journal for Numerical and Analytical Methods in Geomechanics*, 26(6):579–604, 2002.

[4] E. Detournay. Mechanics of hydraulic fractures. *Annual Review of Fluid Mechanics*, 48:311–339, 2016.

[5] E. Donaldson, W. Alam, and N. Begum. *Hydraulic Fracturing Explained: Evaluation, Implementation, and Challenges*. Gulf Drilling. Elsevier Science, 2014.

[6] E. V. Dontsov and A. P. Peirce. A non-singular integral equation formulation to analyse multiscale behaviour in semi-infinite hydraulic fractures. *Journal of Fluid Mechanics*, 781:R1 (11 pages), 10 2015.

[7] J. Dundurs. Elastic interaction of dislocations with inhomogeneities. In T. Mura, editor, *Mathematical Theory of Dislocations*, chapter 4, pages 70–115. The American Society of Mechanical Engineers, New York, N.Y. 10017, 1969.

[8] M. J. Economides, K. G. Nolte, U. Ahmed, and D. Schlumberger. *Reservoir stimulation*, volume 18. Wiley Chichester, 2000.

[9] D. Garagash and E. Detournay. The tip region of a fluid-driven fracture in an elastic medium. *Journal of Applied Mechanics*, 67:1 (10 pages), 6 1999.

[10] D. Garagash, E. Detournay, and J. Adachi. Multiscale tip asymptotics in hydraulic fracture with leak-off. *Journal of Fluid Mechanics*, 669:260–297, 2 2011.

[11] A. Griffith. The phenomena of rupture and flow in solids. *Philosophical Transactions of the Royal Society of London A: Mathematical, Physical and Engineering Sciences*, 221(582-593):163–198, 1921.

[12] D. A. Hills, P. A. Kelly, D. N. Dai, and A. M. Korsunsky. *Solution of crack problems*, volume 44 of *Solid Mechanics and its Applications*. Kluwer Academic Publishers Group, Dordrecht, 1996. The distributed dislocation technique.

[13] J. Hirth. Introduction to the mathematical theory of dislocations. In T. Mura, editor, *Mathematical Theory of Dislocations*, chapter 1, pages 1–24. The American Society of Mechanical Engineers, New York, N.Y. 10017, 1969.

[14] M. F. Kanninen and C. L. Popelar. Advanced fracture mechanics. 1985.

[15] A. M. Linkov. Analytical solution of hydraulic fracture problem for a non-newtonian fluid. *Journal of Mining Science*, 49(1):8–18, 2013.

[16] A. M. Linkov. The particle velocity, speed equation and universal asymptotics for the efficient modelling of hydraulic fractures. *J. Appl. Math. Mech.*, 79(1):54–63, 2015.

[17] J. A. Mechanics, F. E. C. N. U. (1969.), .-e. Mura, Toshio, and A. S. of Mechanical Engineers. Applied Mechanics Division. Mathematical theory of dislocations, 1969. "Sponsored by Applied Mechanics Division of the American Society of Mechanical Engineers.".

[18] T. Mura. Method of continuously distributed dislocations. In T. Mura, editor, *Mathematical Theory of Dislocations*, chapter 2, pages 25–48. The American Society of Mechanical Engineers, New York, N.Y. 10017, 1969.

[19] A. Peirce and E. Detournay. An implicit level set method for modeling hydraulically driven fractures. *Computer Methods in Applied Mechanics and Engineering*, 197(33):2858–2885, 2008.

[20] M. Williams. Stress singularities resulting from various boundary conditions. *Journal of Applied Mechanics*, 19:526–528 (2 pages), 4 1952.

Appendix A

Closed Formulae for two Integrals

A.1 Proof of Closed Form Formula for $\int_0^\infty \frac{G(t)}{t^\alpha} dt$

We will prove the identity

$$J(\alpha) \equiv \int_0^\infty \frac{G(t)}{t^\alpha}\, dt = \frac{2\pi}{\alpha(2-\alpha)} \tan\left(\frac{\pi\alpha}{2}\right), \qquad (-1 < \alpha < 1).$$

Let $0 < \varepsilon \ll 1$ and define

$$J_\varepsilon(\alpha) \equiv \left(\int_0^{1-\varepsilon} + \int_{1+\varepsilon}^\infty\right) \frac{G(t)}{t^\alpha}\, dt = J(\alpha) - \int_{1-\varepsilon}^{1+\varepsilon} \frac{G(t)}{t^\alpha} dt.$$

As $\varepsilon \longrightarrow 0$ we find that the rightmost term is $O(\varepsilon)$ and therefore

$$J_\varepsilon(\alpha) \longrightarrow J(\alpha) \qquad (\varepsilon \longrightarrow 0).$$

Now we write

$$J_\varepsilon(\alpha) = \left(\int_0^{1-\varepsilon} + \int_{1+\varepsilon}^\infty\right) \frac{1-t^2}{t^{1+\alpha}} \left[\log\left|\frac{1+t}{1-t}\right| + \frac{2t}{1-t^2}\right] dt,$$

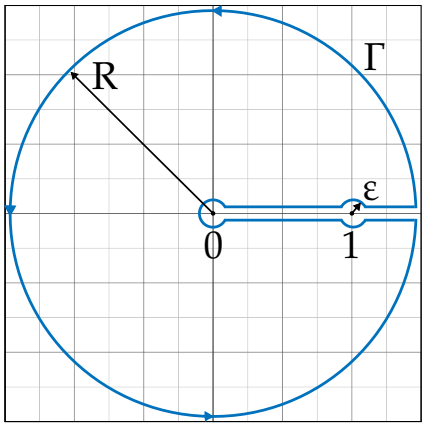

Figure A.1: Schematic of the integration contour.

and integrate by parts to get

$$\begin{aligned} J_\varepsilon(\alpha) = &- \frac{(2-\alpha)t^{-\alpha} + \alpha t^{2-\alpha}}{\alpha(2-\alpha)} \left[\log\left|\frac{1+t}{1-t}\right| + \frac{2t}{1-t^2} \right] \Big|_0^\infty \\ &+ \frac{(2-\alpha)t^{-\alpha} + \alpha t^{2-\alpha}}{\alpha(2-\alpha)} \left[\log\left|\frac{1+t}{1-t}\right| + \frac{2t}{1-t^2} \right] \Big|_{1-\varepsilon}^{1+\varepsilon} \\ &+ \frac{4}{\alpha(2-\alpha)} \left(\int_0^{1-\varepsilon} + \int_{1+\varepsilon}^\infty \right) \frac{(2-\alpha)t^{-\alpha} + \alpha t^{2-\alpha}}{(1-t^2)^2}\, dt \end{aligned}$$

Since $1 < \alpha < 1$ and

$$\log\left|\frac{1+t}{1-t}\right| + \frac{2t}{1-t^2} = \begin{cases} O(t), & \text{as } t \to 0, \\ O(t^{-3}), & \text{as } t \to \infty, \end{cases}$$

the boundary terms at 0 and ∞ vanish. Carrying out the calculation for the boundary terms at $1-\varepsilon$ and $1+\varepsilon$ we obtain a single $O(\varepsilon^{-1})$ term leading to

$$J_\varepsilon(\alpha) = -\frac{4}{\alpha(2-\alpha)} \frac{1}{\varepsilon} + \frac{4}{\alpha(2-\alpha)} \left(\int_0^{1-\varepsilon} + \int_{1+\varepsilon}^\infty \right) \frac{(2-\alpha)t^{-\alpha} + \alpha t^{2-\alpha}}{(1-t^2)^2}\, dt. \tag{A.1}$$

To evaluate the remaining integral we calculate the contour integral

$$\int_\Gamma \frac{(2-\alpha)z^{-\alpha} + \alpha z^{2-\alpha}}{(1-z^2)^2}\, dz,$$

where the contour Γ consists of one large circular contour of radius R centred at $z = 0$ and two small circular contours centred at $z = 0$ and $z = 1$ as shown in Figure A.1. Furthermore we introduce a branch cut along the positive real axis to account for the power z^α. In the limit of $\varepsilon \longrightarrow 0$ the contribution from the small circle at $z = 0$ vanishes and the remaining contributions equal

$$\begin{aligned} O(R^{-\alpha-3})+O(R^{-1-\alpha}) + (1-e^{-i2\pi\alpha})\left(\int_0^{1-\varepsilon} + \int_{1+\varepsilon}^{\infty}\right)\frac{(2-\alpha)t^{-\alpha}+\alpha t^{2-\alpha}}{(1-t^2)^2}\,dt \\ -\int_0^{\pi}\frac{(2-\alpha)(1+\varepsilon e^{i\theta})^{-\alpha}+\alpha(1+\varepsilon e^{i\theta})^{2-\alpha}}{(-2\varepsilon e^{i\theta}-\varepsilon^2 e^{i2\theta})^2}\varepsilon i e^{i\theta}d\theta \\ -e^{-i2\pi\alpha}\int_0^{\pi}\frac{(2-\alpha)(1+\varepsilon e^{-i\theta})^{-\alpha}+\alpha(1+\varepsilon e^{-i\theta})^{2-\alpha}}{(-2\varepsilon e^{-i\theta}-\varepsilon^2 e^{-i2\theta})^2}\varepsilon i e^{-i\theta}d\theta, \end{aligned}$$

where the $O(R^{-\alpha-3})$ and $O(R^{-1-\alpha})$ terms are coming from integrating along the large outer circle. Meanwhile the latter two terms equal $\frac{i\pi}{2} - \frac{1}{\varepsilon}$ and $\frac{i\pi}{2}e^{-i2\pi\alpha} + \frac{1}{\varepsilon}e^{-i2\pi\alpha}$ respectively with an $O(\varepsilon)$ correction. On the other hand, the contour integral can be evaluated using Cauchy's residue theorem which yields $i\pi e^{-i\pi\alpha}$. Combining these results we obtain

$$\left(\int_0^{1-\varepsilon} + \int_{1+\varepsilon}^{\infty}\right)\frac{(2-\alpha)t^{-\alpha}+\alpha t^{2-\alpha}}{(1-t^2)^2}\,dt = \frac{\pi}{2}\tan\left(\frac{\pi\alpha}{2}\right) + \frac{1}{\varepsilon} + O(\varepsilon),$$

whence

$$J_\varepsilon(\alpha) = \frac{2\pi}{\alpha(2-\alpha)}\tan\left(\frac{\pi\alpha}{2}\right) + O(\varepsilon),$$

and the desired result follows by taking the limit $\varepsilon \to 0$.

A.2 Proof of Closed Form Formula for $\int_0^\infty \frac{G'(t)}{t^\kappa}dt$

We will prove the identity

$$\int_0^\infty \frac{G'(t)}{t^\kappa}\,dt = \frac{2\pi\kappa}{(1+\kappa)(1-\kappa)}\tan\left(\frac{\pi}{2}(\kappa+1)\right) \qquad (-2 < \kappa \leq 0).$$

First, we consider the case $-2 < \kappa < 0$. Integrating by parts and using $G(t) \sim O(1)$ as $t \to 0$ and $G(t) \sim O(t^{-2})$ as $t \to \infty$ to cancel the boundary terms we obtain

$$\int_0^\infty \frac{G'(t)}{t^\kappa}\, dt = \kappa \int_0^\infty \frac{G(t)}{t^{\kappa+1}}\, dt.$$

Since $-1 < \kappa + 1 < 1$ we can use the identity (4.9) from which the desired result follows.

When $\kappa = 0$ we obtain

$$\int_0^\infty G'(t)dt = G(\infty) - G(0) = -4,$$

which agrees with the desired identity upon setting $\kappa = 0$.

Appendix B

Matlab Code

B.1 Newton's Method Solver for Non-Singular Integral Equation

```
function [xt,wt,wta,itt,Res,totTime,odeTime] =
    MKC_calc_w(n,chi,p0,p1,N,ittmax,tol)
% ------------------------ Preamble ----------------------------------------
%
% DESCRIPTION:
%  This function solves for $\tilde{w}(\tilde{x})$ by first discretizing
%  the non-linear integral equation using Simpson's rule and then solving
%  the resulting non-linear system of equations using Newton's method. The
%  initial guess used for Newton's method comes from solving the linear
%  approximating ODE using ode45.
%
% INPUTS:
%  n       - flow behaviour index
%  chi     - leakoff parameter
%  p0,p1   - powers determining range of xt via 10^p0 < xt < 10^p1
%  N       - number of intervals for Simpsons rule (note length(xt)=2*N+1)
%  ittmax  - maximum number of iterations in Newton's method
%  tol     - desired relative tolerance in Newton's method
%
% OUTPUTS:
%  xt      - \tilde{x} values (logarithmically distributed)
%  wt      - the solution $\tilde{w}$
%  wta     - solution of the approximating ODE
%  itt     - number of iterations before Newton's method termianted
```

```
%  Res     - maximum relative change during last iteration
%  totTime - total computation time

% ------------------------ Initialization ---------------------------------

% initiate the Matlab timer
tic

% generate logarithmically distributed nodes for $\tilde{xt}$
xt = logspace(p0,p1,2*N+1);

% beta_m for the viscous regime
if n == 0
    beta_m = 2*sqrt(pi);
else
    beta_m = (-2*((n+2)^2)/(n*cot(2*pi/(n+2))))^(1/(n+2));
end

% -------------------- Infinity Residual Computation ---------------------

% initialize infinity residual vector
I_inf = zeros(length(xt),1);

% infinity residual for X_i < X_{2N+1}
I_inf(1:1:end-1) = (8/pi)*(4*(2+n)/(3*(beta_m^(n+1))*(2+3*n)))...
                  *(xt(1:1:end-1)'.^2)./(xt(end)^((2+3*n)/(2+n)));

% coefficient calculation for X_i = X_{2N+1}
M = 20;
n_par = 2*n/(2+n);
Coeff_Sum = 1/(3*(1+n_par));
for k=1:1:M
    Coeff_Sum = Coeff_Sum + 1/((2*k+1*n_par)*(2*k+1)*(2*k+3));
end

% infinity residual for X_i = X_{2N+1}
I_inf(end) = (8/pi)*(4*Coeff_Sum/(beta_m^(n+1)))*(xt(end)^((2-n)/(2+n)));

% ---------- Initial Approximation for Newton's Method -------------------

% solve approximating linear ODE
if (chi == 0) || (n == 0)
    % exact solution available for n = 0 and chi = 0
    wta = (1 + (beta_m^(2+n))*xt.^(2-n)).^(1./(2+n))';
else
    % solve numerically using ode45

    % calculate ODE coefficients
```

```
    g1 = -2*(4-n^2)*tan(2*pi/(2+n))/n;
    g2 = -32*(2-n)*(1+n)*tan(pi*(4+n)/(4*(1+n)))/(3*n*(4+n));

    % solve the constant delta approximating ODE using ode45
    odefun = @(x,w) ((1+chi./w).^(n-1)).*(g1./w.^(1+n) +
        chi*g2./w.^(2+n)).*x.^(1-n);
    [~,wta] = ode45(@(X,W)odefun(X,W),[0,xt],1);
    wta = wta(2:end);

end

odeTime = toc;

% ---------- Simpson's Rule Set Up ----------------------------------------

% ds^(2-n)/(2-n) for Simpson's rule
ds = zeros(2*N+1,1);
ds(1) = xt(3)^(2-n) - xt(1)^(2-n);
ds(2:2:2*N) = 4*(xt(3:2:2*N+1).^(2-n)-xt(1:2:2*N-1).^(2-n));
ds(3:2:2*N-1) = xt(5:2:2*N+1).^(2-n)-xt(1:2:2*N-3).^(2-n);
ds(2*N+1) = xt(2*N+1)^(2-n) - xt(2*N-1)^(2-n);
ds = ds/(6*(2-n));

% matrix with G values
[ST,XT] = meshgrid(xt,xt);
G = func_G(ST./XT);

% matrix representing the discretized kernel as a linear operator
[dS,~] = meshgrid(ds,ds);
B = (8/pi)*G.*dS;

% ---------- Newton's Method Solver ---------------------------------------

% initialize Newton's method
Res = 1;
itt = 0;
wt = wta;

% main loop for Newton's method
while (Res>tol)&&(itt<ittmax)
    % incremenet iteration counter
    itt=itt+1;

    % check if maximum allowable iterations have been reached
    if itt==ittmax-1
      disp('No convergence, MKC2');
      disp(Res);
    end
```

```
    % non-linear algebraic equation (solving F = 0)
    F = 1 - wt + B*((1./wt.^(n+1)).*((1+chi./wt).^n)) + I_inf;

    % calculate Jacobian of F for Newton's method
    J = -1*(n+1)*B*diag((1./wt.^(n+2)).*((1+chi./wt).^n)) ...
        - chi*n*B*diag((1./wt.^(n+3)).*((1+chi./wt).^(n-1))) ...
        - eye(length(wt));

    % calculate next iterated solution
    wt_temp = wt - J\F;

    Res = max(abs(wt_temp-wt)./wt_temp);
    wt = wt_temp;
end

% total elapsed time
totTime = toc;

end
```

B.2 Zero Delta-Corrected Solution

```
function [ xt0 ] = fcnV_xt0(wt,chi,n)
% vectorized xt0 function

% make sure wt is a column vector
N = length(wt);
wt = reshape(wt,N,1);

if n ~= 0
    % n != 0 case

    % load Gaussian Quadrature points and weights
    gauss_quad = get_gauss();
    quad_weights = gauss_quad(:,1);
    quad_points = gauss_quad(:,2);
    M = length(quad_weights);

    % constants for zero-order solution
    g1 = -2*(4-n^2)*tan(2*pi/(2+n))/n;
    g2 = -32*(2-n)*(1+n)*tan(pi*(4+n)/(4*(1+n)))/(3*n*(4+n));
    b0 = g2/g1;

    % change of variables coefficients
```

```
    A = 0.5*(wt-1); B = 0.5*(wt+1);

    % change of variables evaluated at the quadrature points
    V = A*quad_points'+B*ones(1,M);

    % integrand in matrix form
    J0 = (V+chi).^(1-n).*V.^(1+2*n)./(V+b0*chi);

    % zero-order solution (n ~= 0)
    xt0 = (((2-n)/g1)*A.*(J0*quad_weights)).^(1./(2-n));

else
    % zero-order solution (n == 0)
    xt0 = 0.5*((wt.^2-1)./pi).^0.5;

end

end
```

B.3 First Delta-Corrected Solution

```
function [ xt1 ] = fcnV_xt1(wt,chi,n)
% function [ xt2, C1, C2 ] = fcnV_xt1(wt,chi,n)
% vectorized xt1 function

% make sure wt is a column vector
N = length(wt);
wt = reshape(wt,N,1);

if n ~= 0
    % n != 0 case

    % load Gaussian Quadrature points and weights
    gauss_quad = get_gauss();
    quad_weights = gauss_quad(:,1);
    quad_points = gauss_quad(:,2);
    M = length(quad_weights);

    % constants for zero-order solution
    g1 = -2*(4-n^2)*tan(2*pi/(2+n))/n;
    g2 = -32*(2-n)*(1+n)*tan(pi*(4+n)/(4*(1+n)))/(3*n*(4+n));
    b0 = g2/g1;

    % first delta-correction
    d1 = (g1./(1+chi./wt).^(1-n)).*(fcnV_xt0(wt,chi,n).^(2-n)./...
```

```
                    wt.^(2+n)).*(1+chi.*b0./wt);

    % constants for first-delta iteration
    C1 = 16*(2-n-(n+1).*d1).*tan(0.5*pi*(1-n-(n+1).*d1))./((1-n-(n+1).*d1)...
        .*(3-n-(n+1).*d1));
    C2 = 16*(2-n-(1+2*n).*d1).*tan(0.5*pi*(1-n-(1+2*n).*d1))./((1-n-(1+2*n)...
        .*d1).*(3-n-(1+2*n).*d1));

    % change of variables coefficients
    A = 0.5*(wt-1); B = 0.5*(wt+1);

    % change of variables evaluated at the quadrature points
    V = A*quad_points'+B*ones(1,M);

    % integrand in matrix form
    J1 = (V+chi).^(1-n).*V.^(1+2*n)./...
          (V.*(C1*ones(1,M))+chi*C2*ones(1,M));

    % first-delta-corrected solution (n ~= 0)
    xt1 = ((2-n)*A.*(J1*quad_weights)).^(1./(2-n));

else
    % n = 0 case

    % first delta-correction
    d1 = (wt.^2-1)./wt.^2;

    % constant for first-delta correction
    C0 = 16.*(2-d1).*tan(0.5*pi*(1-d1))./((1-d1).*(3-d1));
    C0(abs(1-d1)<1e-6) = 4*pi*ones(size(C0(abs(1-d1)<1e-6)));

    % first-delta-corrected solution (n == 0)
    xt1 = ((wt.^2-1)./C0).^0.5;

end
```